

## THE SIZE EVOLUTION OF GALAXIES SINCE $z \sim 3$ : COMBINING SDSS, GEMS AND FIRES<sup>1</sup>

IGNACIO TRUJILLO<sup>2,3</sup>, NATASCHA M. FÖRSTER SCHREIBER<sup>4</sup>, GREGORY RUDNICK<sup>5</sup>, MARCO BARDEN<sup>2</sup>, MARIJN FRANX<sup>6</sup>, HANS-WALTER RIX<sup>2</sup>, J. A. R. CALDWELL<sup>7</sup>, DANIEL H. MCINTOSH<sup>8</sup>, SUNE TOFT<sup>9</sup>, BORIS HÄUSSLER<sup>2</sup>, ANDREW ZIRM<sup>6</sup>, PIETER G. VAN DOKKUM<sup>9</sup>, IVO LABBÉ<sup>10</sup>, ALAN MOORWOOD<sup>11</sup>, HUUB RÖTTGERING<sup>6</sup>, ARJEN VAN DER WEL<sup>6</sup>, PAUL VAN DER WERF<sup>6</sup>, LOTTIE VAN STARKENBURG<sup>6</sup>

*To appear in ApJ.*

### ABSTRACT

We present the evolution of the luminosity–size and stellar mass–size relations of luminous ( $L_V \gtrsim 3.4 \times 10^{10} h_{70}^{-2} L_\odot$ ) and of massive ( $M_* \gtrsim 3 \times 10^{10} h_{70}^{-2} M_\odot$ ) galaxies in the last  $\sim 11$  Gyr. We use very deep near–infrared images of the Hubble Deep Field–South and the MS1054–03 field in the  $J_s$ , H and  $K_s$  bands from FIRES to retrieve the sizes in the optical rest–frame for galaxies with  $z > 1$ . We combine our results with those from GEMS at  $0.2 < z < 1$  and SDSS at  $z \sim 0.1$  to achieve a comprehensive picture of the optical rest–frame size evolution from  $z=0$  to  $z=3$ . Galaxies are differentiated according to their light concentration using the Sérsic index  $n$ . For less concentrated objects, the galaxies at a given luminosity were typically  $\sim 3 \pm 0.5$  ( $\pm 2 \sigma$ ) times smaller at  $z \sim 2.5$  than those we see today. The stellar mass–size relation has evolved less: the mean size at a given stellar mass was  $\sim 2 \pm 0.5$  times smaller at  $z \sim 2.5$ , evolving proportional to  $(1+z)^{-0.40 \pm 0.06}$ . Simple scaling relations between dark matter halos and baryons in a hierarchical cosmogony predict a stronger (although consistent within the error bars) than observed evolution of the stellar mass–size relation. The observed luminosity–size evolution out to  $z \sim 2.5$  matches well recent infall model predictions for Milky–Way type objects. For low- $n$  galaxies, the evolution of the stellar mass–size relation would follow naturally if the individual galaxies grow inside–out. For highly concentrated objects, the situation is as follows: at a given luminosity, these galaxies were  $\sim 2.7 \pm 1.1$  times smaller at  $z \sim 2.5$  (or put differently, were typically  $\sim 2.2 \pm 0.7$  mag brighter at a given size than they are today), and at a given stellar mass the size has evolved proportional to  $(1+z)^{-0.45 \pm 0.10}$ .

*Subject headings:* galaxies: fundamental parameters, galaxies: evolution, galaxies: high redshift, galaxies: structure

### 1. INTRODUCTION

Over the last few decades (starting with Fall & Efstathiou 1980 and Fall 1983) there has been a substantial effort towards understanding, theoretically and through observations, how galaxies have reached their current sizes over cosmic time. The answer to this question plays a key role in our understanding of galaxy formation and evolution.

Several approaches have been tried to make specific predictions about how sizes of galaxies (particularly the

disk galaxies) evolves with redshift: semi–analytical hierarchical models, direct numerical simulations and infall models.

The semi–analytical hierarchical model assumes simple scaling relationships between the properties of the galaxy disks and the halos in which they reside (Lacey et al. 1993; Kauffmann & Charlot 1994; Dalcanton et al. 1997; Mo, Mao & White 1998; Somerville & Primack 1999; van den Bosch 2000; Cole et al. 2000; Naab & Ostriker 2006). According to this picture, galaxy disks are formed from gas with some initial angular momentum that cools and contracts in dark matter halos. The mass and the angular momentum that settle in the disk are some fixed fractions of the mass and the angular momentum of the halo respectively. The mass and size of the halos are tightly linked to the density of the universe at the time the halos were formed; consequently, halos formed at high- $z$  are expected to be much denser than halos formed at lower  $z$ . Under the assumption that the fractions of disk mass and angular momentum in the disk relative to the halo, together with the spin parameter of the halo do not vary with redshift, Mo et al. suggest the following redshift scaling for the size of the baryonic disk at their *formation* redshift:  $R \propto H^{-1}(z)$  at a fixed circular halo velocity or  $R \propto H^{-2/3}(z)$  at a fixed halo mass, where  $H(z)$  is the Hubble constant at a given  $z$ :  $H(z) = H_0 [\Omega_m (1+z)^3 + \Omega_\Lambda]^{1/2}$  in a flat Universe.

High–resolution N–body/gas–dynamical simulations (Navarro & Steinmetz 2000; Brook et al. 2006) find that the above picture is too simplistic; e.g. large system–

<sup>1</sup> Based on observations collected at the European Southern Observatory, Paranal, Chile (ESO LP 164.O–0612). Also, based on observations with the NASA/ESA *Hubble Space Telescope*, obtained at the Space Telescope Science Institute, which is operated by AURA Inc, under NASA contract NAS 5–26555.

<sup>2</sup> Max-Planck-Institut für Astronomie, Königstuhl 17, 69117 Heidelberg, Germany

<sup>3</sup> School of Physics & Astronomy, University of Nottingham, University Park, Nottingham, NG7 2RD, UK

<sup>4</sup> Max-Planck-Institut für extraterrestrische Physik, Giessenbachstrasse, D-85748, Garching, Germany

<sup>5</sup> NOAO, 950 N. Cherry Av. Tucson AZ 85719

<sup>6</sup> Leiden Observatory, P.O. Box 9513, NL–2300 RA, Leiden, The Netherlands

<sup>7</sup> University of Texas, McDonald Observatory, Fort Davis, TX 79734

<sup>8</sup> Astronomy Department, University of Massachusetts, 710 N. Pleasant St., Amherst, MA 01003

<sup>9</sup> Department of Astronomy, Yale University, P.O. Box 208101, New Haven, CT 06520–8101

<sup>10</sup> Carnegie Observatories, 813 Santa Barbara Street, Pasadena, CA 91101

<sup>11</sup> European Southern Observatory, D–85748, Garching, Germany

atic variations in the fraction of baryons that collapse to form galaxies are observed and angular momentum conservation may not hold. Moreover, the explanation of the observed local size–mass relation within this hierarchical context (Shen et al. 2003) requires that the above scaling between the dark matter and baryons is broken and instead that the fraction of baryons in the disk is a function of the halo mass. This is also predicted by standard feedback models based on galactic winds.

The infall model approach (Cayón, Silk & Charlot 1996; Bouwens, Cayón & Silk 1997) examines a number of local disk galaxies in great detail and uses detailed models of their observed properties, e.g. gas profiles, stellar profiles, metallicity profiles, current star formation rate (SFR), and age–metallicity relationships, to infer how galaxies might have evolved from high redshift. This approach uses the local universe as a reference and consequently does not explain why the local galaxy population is as it is. The main ingredients of these models are: a) that the SFR is determined at each radius and time from the local gas density according to a Schmidt–type law, and b) that metal–free gas infalls with certain time-scale. Using the Milky Way as reference, Bouwens & Silk (2002) provide the following size scaling relationship with redshift:  $R(z)/R(0)=1-0.27z$ .

In the case of spheroid–dominated galaxies, they are expected to form from the merging of smaller systems (White & Frenk 1991) and consequently to have a different size evolution than disk–dominated systems. The old stellar populations found in nearby ellipticals make it unlikely that these galaxies were the remnant of a merger between two similar spirals drawn from the observed local population. In fact, Khochfar & Burkert (2003) have shown that dissipationless mergers of early–type galaxies may dominate the formation of the nowadays high–mass early–type galaxies. In addition, there is some observational (van Dokkum 2005; Tran et al. 2005; Bell et al. 2006) and theoretical (Naab, Khochfar & Burkert 2006; Boylan–Kolchin et al. 2006) evidence pointing towards the merger of red galaxies as the potential formation mechanisms for the spheroid population. Shen et al. (2003) have shown that the present–day stellar mass–size relation for early–type galaxies follows  $R \propto M^{0.56}$ . Shen et al. indicate that the present–day relation is consistent with a model where early–type galaxies are the remnants of repeated mergers where the progenitors have properties similar to those of faint ellipticals. According to their model, the size of the remnant increases after each merger. In this context, we would expect that early–type galaxies that have undergone a major merger were larger in size than galaxies of the same mass that have not suffered such a process.

Detailed modeling of the merger histories of galaxies in the cold dark matter scenario suggests that the last major merging event is typically around redshift unity (Kauffmann & Haehnelt 2000). Consequently, we would expect that the sizes of early–type galaxies at  $z>1$  were, in general, smaller than the local counterparts. An analysis of the evolution of the stellar mass–size relation at high– $z$  of these objects can constrain the above scenario of merging formation.

Historically, the monolithic collapse scenario (Eggen, Lynden–Bell & Sandage 1962; Larson 1975) envisioned that all spheroidal galaxies formed very early via a rapid

collapse of the gas at high redshift. In this picture, E/S0s would already be in place at high– $z$  and we would expect then that the changes in the observed properties of early–type galaxies over time were due to simple passive fading of their stellar populations. The more modern version of this scenario (e.g. Chiosi & Carraro 2002; Merlin & Chiosi 2006) envisions that massive ellipticals also formed hierarchically, but at quite high redshift.

The evolution of individual galaxies is not directly observable. However, look–back studies can provide extensive information on how the population properties of galaxies have changed with cosmic epoch. Early studies (Smail et al. 1995; Casertano et al. 1995; Roche et al. 1998) showed that galaxies at a given luminosity were smaller in the past. However, it was not until the application of the Lyman–break technique (Steidel et al. 1996) that the study of a large number of galaxies at high– $z$  was possible. This technique is especially efficient at selecting star–forming galaxies at  $z>2$ . Sizes have been measured for these Lyman Break Galaxies (LBGs) (Giavalisco, Steidel & Macchetto 1996; Lowenthal et al. 1997; Ferguson et al. 2004), but using optical filters, i.e. measuring their sizes in the rest–frame ultraviolet (UV) region of their spectra. At these wavelengths the LBGs appear compact ( $r \sim 0.''2-0.''3$ ,  $\sim 1.5-2.5 h_{70}^{-1}$  kpc). However, there is some evidence that the LBG morphology depends very little on the wavelength, remaining essentially unchanged from the far–UV to the optical window (Giavalisco 2002; Papovich et al. 2005).

As a result of the dearth of very deep near–infrared (NIR) images, most of the studies using the rest–frame optical have been limited in redshift up to  $z \sim 1$  (Schade et al. 1996; Lilly et al. 1998; Simard et al. 1999; Ravindranath et al. 2004; Trujillo & Aguerri 2004; McIntosh et al. 2005; Barden et al. 2005). To properly compare with local optically selected samples and to trace the size evolution in a consistent fashion at  $z>1$  one needs to use very deep NIR data. Consequentially any observed size evolution would then reflect true evolutionary changes not subject to the changing appearance of galaxies in different bandpasses. Moreover, it seems now clear that rest–frame UV selected samples do not provide a complete census of the galaxy population at high– $z$  (e.g. Franx et al. 2003; van Dokkum et al. 2003; Daddi et al. 2004) and, in particular, a substantial population of red objects are missing from purely rest–frame UV selected surveys.

In addition to the use of rest–frame optical sizes, it would be of great help to facilitate a direct comparison with the theoretical expectations if the size evolution could be measured at a given mass rather than a given luminosity. Using circular velocity measurements to estimate galaxy masses at high– $z$  is difficult and few objects have been analyzed (see e.g. Vogt et al. 1996; 1997; Boehm & Ziegler 2006; Erb et al. 2006). An alternative approach is to estimate the stellar masses from their rest–frame colors and spectral energy distributions (SEDs).

With the above ideas in mind we performed an exploratory work (Trujillo et al. 2004) to probe the evolution of the luminosity–size and stellar mass–size relations of the galaxies out to  $z \sim 3$ . That work used very deep NIR images of the Hubble Deep Field–South (HDF–S) from the Faint Infrared Extragalactic Survey (FIRES; Franx et al. 2000). We found that the rest–frame V–band

sizes of luminous galaxies ( $\langle L_V \rangle \sim 4 \times 10^{10} h_{70}^{-2} L_\odot$ ) at  $2 < z < 3$  were 3 times smaller than for equally luminous galaxies today. In contrast, the stellar mass–size relation had evolved relatively little: the size of galaxies more massive than  $2 \times 10^{10} h_{70}^{-2} M_\odot$ , were  $\sim 1.5$  times smaller at  $z \sim 2.5$ <sup>12</sup>.

In the present work we add to the above data set the results from the analysis of the  $\sim 4$  times larger MS1054–03 FIRES field. Using both FIRES fields we decrease the effects of the field–to–field variations in our results and multiply by three the number of objects with  $z > 1$  in our sample. In addition, we make a detailed comparison of our results with those found in the Sloan Digital Sky Survey (SDSS; York et al. 2000) at  $z \sim 0.1$  and in the Galaxy Evolution from Morphology and SEDs (GEMS; Rix et al. 2004) survey at intermediate redshift  $0.2 < z < 1$ . This allows us to follow in detail the evolution of the luminosity–size and stellar mass–size relations of the luminous galaxies over the last  $\sim 11$  Gyr.

The structure of this paper is as follows. In Sect. 2 we describe the FIRES data, and in Sect. 3 the size measurement technique and robustness estimations for the FIRES data. In Sect. 4 we present the observed luminosity–size and stellar mass–size relations and compare our results with other samples in Sect. 5. We discuss our results in Sect. 6.

All magnitudes in this paper are given in the AB system unless otherwise stated. Throughout, we will assume a flat  $\Lambda$ -dominated cosmology ( $\Omega_M = 0.3$ ,  $\Omega_\Lambda = 0.7$  and  $H_0 = 70 \text{ km s}^{-1} \text{ Mpc}^{-1}$ ).

## 2. FIRES: DATA

The data used here were obtained as part of FIRES (Franx et al. 2000), a non–proprietary NIR survey of the HDF–S and MS 1054–03 fields carried out at the European Southern Observatory (ESO) Very Large Telescope (VLT). The data processing and photometry are discussed in detail by Labbé et al. (2003a) for HDF–S and Förster Schreiber et al. (2005) for the MS 1054–03 field<sup>13</sup>.

The NIR images were obtained using the VLT Infrared Spectrograph And Array Camera (ISAAC; Moorwood et al. 1997). The HDF–S was imaged for 33.6 hr in  $J_s$ , 32.3 hr in  $H$ , and 35.6 hr in  $K_s$  in a single  $2.5 \times 2.5$  pointing covering the Hubble Space Telescope (HST) WFPC2 main field. The NIR data were complemented with deep optical publicly available HST WFPC2 imaging in the  $U_{300}$ ,  $B_{450}$ ,  $V_{606}$  and  $I_{814}$  bands (Casertano et al. 2000). For the MS 1054–03 field, 77 hr of ISAAC integration time was obtained in a  $5' \times 5'$  mosaic of four pointings. Already existing mosaics in the WFPC2  $V_{606}$  and  $I_{814}$  bands (van Dokkum et al. 2000) were used. In addition, Bessel U, B, and V band imaging with the VLT FORS1 instrument were collected.

<sup>12</sup> During the writing of the present paper we discovered a bug in the code which was used to estimate the sizes in the 2004 paper. The sizes of the smallest objects in our HDF–S sample ( $r_e < 0.2''$ ) were overestimated. This produced a slight underestimation on the degree of evolution in the luminosity and stellar mass size relation. This problem has been solved in the present version.

<sup>13</sup> The reduced images, photometric catalogs, photometric redshift estimates, and rest–frame luminosities are available online through the FIRES home page at <http://www.strw.leidenuniv.nl/~fires>.

The depth ( $3 \sigma$ ) reached was 26.8 mag in  $J_s$ , 26.2 mag in  $H$ , and 26.2 mag in  $K_s$  for point sources in the HDF–S. The MS 1054–03 field surveys an area four times larger down to  $\sim 0.7$  mag brighter magnitudes. The effective seeing in the reduced images is approximately  $0.''47$  in all NIR bands in the HDF–S and  $0.''49$  in the MS 1054–03 field.

The sources were selected in the  $K_s$  band using version 2.2.2 of the SExtractor software (Bertin & Arnouts 1996). For consistent photometry across all bands, the fluxes were measured on the maps convolved to a common spatial resolution, matching the map of poorest seeing. Colours and spectral energy distributions used in this work are based on measurements in custom isophotal apertures defined from the detection map. Total magnitudes in the  $K_s$  band were computed in apertures based on autoscaling apertures (Kron 1980) for isolated sources and adapted isophotal apertures for blended sources. The photometric uncertainties were derived empirically from simulations on the maps.

K band selected samples ensure, for  $z \lesssim 3$  galaxies, a selection based on flux at wavelengths redder than the rest–frame V band. This selection is less sensitive to unobscured star formation than selections based in the rest–frame UV bands. From the above K band catalogs we removed stars if their spectral energy distributions (SEDs) were better fitted by a single stellar template than by a linear combination of galaxy templates. In the HDF–S two obviously extended objects were removed from the star lists and in the MS1054–03 field, 4 bright spectroscopically identified stars were added to the star lists.

Photometric redshifts  $z_{ph}$ , as well as the rest–frame optical luminosities, were estimated by fitting a linear combination of redshifted SEDs of galaxies of various types (Rudnick et al. 2001, 2003). Comparison with available spectroscopic redshifts  $z_{sp}$  implies an accuracy of  $\delta z \equiv |z_{sp} - z_{ph}| / (1 + z_{sp}) >= 0.074$  for both fields. When possible, spectroscopic redshifts were used.

To ensure sufficient signal–to–noise ratio for the subsequent size determinations we selected only galaxies with  $K_s \leq 23.5$  in the HDF–S and  $K_s \leq 23$  in the MS 1054–03 field and whose fractional exposure time in all the filters were larger than 15% of the maximum in each field. This leaves us with a total sample of 171 objects in the HDF–S and 708 in the MS 1054–03 field. In part, the large number of objects in the MS 1054–03 field is caused by a “foreground” cluster at  $z = 0.83$ . To avoid possible contamination in our field galaxy analysis by cluster galaxies we select only objects with  $z \geq 1$ . This is particularly effective at bright magnitudes due to the high spectroscopic completeness for cluster members. For homogeneity, the same  $z$  cut is used in the HDF–S in the present work.

The final number of galaxies used in this paper is 87 in the HDF–S and 175 in the MS 1054–03 field.

The stellar mass–to–light (M/L) ratio and hence the stellar masses of the objects are estimated by Rudnick et al (2006), using rest–frame (B–V) color and SEDs similar to that of Bell & de Jong (2001). We use the relation between color and M/L, which exists over a wide range of monotonic star formation histories and is rather robust against the effects of age, dust extinction, or metallicity. The largest systematic errors in the derived stellar mass

will occur for galaxies with strong ongoing bursts.

### 3. FIRES: REST-FRAME SIZE ESTIMATIONS

The galaxy sizes used in this paper are measured in the observed band that is closest to the rest-frame V-band at every redshift; this means  $J_s$  for galaxies with  $1 < z < 1.5$ , H for galaxies with  $1.5 < z < 2.6$  and  $K_s$  for galaxies with  $2.6 < z < 3.2$ . In addition, we have also measured the sizes of all our galaxies in the  $K_s$  band to analyze the completeness of the sample and test the robustness of the retrieved structural parameters. The structural properties of the galaxies are estimated from a Sérsic (1968)  $r^{1/n}$  model convolved with the image point-spread function (PSF) using the two-dimensional fitting code GALFIT (Peng et al. 2002). The PSF (in all the NIR bands) is very stable with a standard deviation in the FWHM  $< 3\%$  throughout the explored field of view. Best-fitting stellar parameters are summarized in Table 1. The Sérsic model is given by

$$I(r) = I(0) \exp \left[ -b_n \left( \frac{r}{r_e} \right)^{1/n} \right], \quad (1)$$

where  $I(0)$  is the central intensity and  $r_e$  the effective radius enclosing half of the flux from the model light profile. The quantity  $b_n$  is a function of the radial shape parameter  $n$  – which defines the global curvature in the luminosity profile – and is obtained by solving the expression  $\Gamma(2n) = 2\gamma(2n, b_n)$ , where  $\Gamma(a)$  and  $\gamma(a, x)$  are respectively the gamma function and the incomplete gamma function (see Graham & Driver 2005 for a recent review of the Sérsic model).

The Sérsic model is a flexible parametric description of the surface brightness distribution of the galaxies and contains the exponential ( $n=1$ ) and de Vaucouleurs ( $n=4$ ) models as particular cases. In addition, this model is used in the structural analysis of the SDSS galaxy sample (our local comparison sample; Blanton et al. 2003; Shen et al. 2003) and the GEMS data (our comparison sample for galaxies in the redshift range  $0.2 < z < 1$ ; Barden et al. 2005; McIntosh et al. 2005).

GALFIT convolves Sérsic profile galaxy models with the PSF of the images and then determines the best fit by comparing the convolved models with the science data using a Levenberg–Marquardt algorithm to minimize the  $\chi^2$  of the fit. Neighboring galaxies were excluded from each model fit using a mask, but in the case of closely neighboring galaxies with overlapping isophotes, the galaxies were fitted simultaneously.

In what follows, we refer to the “circularized effective radius” of the fitted model, i. e.,  $r_e = a_e \sqrt{1 - \epsilon}$ , where  $a_e$  is the semimajor effective radius (directly measured in our fits) and  $\epsilon$  the intrinsic (non-seeing affected) projected ellipticity of the galaxy. The results of our fitting are shown in Table 3 for the MS1054-03 data. For consistency, the HDF-S data estimated using GALFIT are also provided here (Table 4).

#### 3.1. Structural Parameter Estimates

##### 3.1.1. Simulations

The results presented in this paper rely on our ability to measure accurate structural parameters. To gauge the accuracy of our parameter determination we have created

1000 artificial galaxies uniformly generated at random in the following ranges:  $18 \leq K_s(\text{AB}) \leq 24$ ,  $0.''03 \leq r_e \leq 3''$ ,  $0.5 \leq n \leq 8$  and  $0 \leq \epsilon \leq 0.8$ . To simulate the real conditions of our observations, we add a background sky image (free of sources) taken from a piece of the MS1054 field image in the  $K_s$  band. Finally, the galaxy models were convolved with the observed PSF. The same procedure was used to retrieve the structural parameters both in the simulated and actual images.

The results of these simulations are shown in Figs. 1 and 2. Towards fainter apparent magnitude the parameters recovered are systematically worse. At increasing magnitude the code recovers systematically lower Sérsic indexes. The bias depends strongly on the shape of the surface brightness profiles. We illustrate this by separating the galaxies between less light concentrated profiles ( $n_{\text{input}} < 2.5$ ) and highly concentrated profiles ( $n_{\text{input}} > 2.5$ ). Galaxies with larger  $n$  are more biased than those with lower values.

To illustrate the magnitude of the biases in the different parameters we summarize the results for the most affected bin,  $K_s = 22.5$  mag. For galaxies with  $n_{\text{input}} < 2.5$  we find the following systematics:  $1(\pm 3)\%$  lower luminosities,  $0(\pm 20)\%$  lower sizes,  $30(\pm 23)\%$  lower Sérsic indices. For galaxies with  $n_{\text{input}} > 2.5$ :  $15(\pm 16)\%$  lower luminosities,  $10(\pm 37)\%$  lower sizes,  $52(\pm 21)\%$  lower Sérsic indices. At brighter magnitudes the structural parameters are recovered more accurately.

As shown in Fig. 2 the systematic errors in the structural fitting parameters depend on the apparent magnitude,  $r_e$  and  $n$ . To facilitate the discussion of these biases in our results (see Sect. 4.3) we have quantified analytically what is the relation between the input and output structural parameters depending on the magnitude,  $r_e$  and  $n$  by fitting the following expressions:  $r_{e,\text{out}} = p r_e \times r_{e,\text{input}}^{q r_e}$  and  $n_{\text{out}} = p n \times n_{\text{input}}^{q n}$  to the results of our simulations. The values of  $p$  and  $q$  obtained from the fittings are summarized in Table 2. The difference between the input and output magnitudes has also been quantified as a function of the input magnitude and the index  $n$  (see first row of Fig. 1). It must be mentioned, however, that the effect on the luminosities of our objects is very small  $\lesssim 15\%$  in all the cases (i.e.  $\lesssim 0.15$  mag). We correct the magnitudes according to the following expression  $K_{\text{out}} = p_m + K_{\text{input}}$ . The above expressions allow us to transform from the three elements set ( $K_{s,\text{observed}}$ ,  $r_{e,\text{observed}}$ ,  $n_{\text{observed}}$ ) to ( $K_{s,\text{corrected}}$ ,  $r_{e,\text{corrected}}$ ,  $n_{\text{corrected}}$ ). We have used only the above corrections in Sect. 4.3 to discuss how robust are our results. The results shown in the rest of the paper are based on the directly measured quantities without any attempt to correct the measured parameters in order not to artificially increase the scatter.

It is important to note that although the seeing half-radius ( $\sim 0.3''$ ) is similar to the effective radii of the galaxies we are dealing with, we can estimate reasonable structural parameters due to the depth of our images. Galaxies at our  $K_s = 23$  mag analysis limit are a full 3 magnitudes brighter than our  $3\sigma$  limit for point sources. This allows us to explore the surface brightness radial profiles to 2.5–3 times the seeing half-light radius.

##### 3.1.2. Comparison between different filters

Mock galaxies are useful to estimate the biases on the recovered structural parameters. However, one can argue that because artificial galaxies are simplistic representations of real galaxies, the errors and bias determinations yield lower limits to the real case. We have checked the internal consistency of our data, comparing the size and shape of our galaxies between the set of near infrared filters used. The seeing and the depth are slightly different amongst the NIR images which allows us to have a robustness test which is not based on simulations. Naturally, this test is only useful under the assumption that the change in the size and the shape of the light profile of the galaxies due to changes in the wavelength along the set of NIR filters is smaller than the intrinsic error in estimating the structural parameters.

Fig. 3 shows the comparison between the sizes and the Sérsic indexes estimated in the  $K_s$  band versus the sizes and the Sérsic indexes estimated using  $J_s$  ( $1 < z < 1.5$ ) and H ( $1.5 < z < 2.6$ ) bands for galaxies of the MS1054 field with  $1 < z < 2.6$ . The sizes estimated using the different filters present a  $\sim 24\%$  ( $1\sigma$ ) of relative scatter between them whereas the scatter for the shapes is larger ( $\sim 60\%$ ).

### 3.1.3. Comparison using different PSFs

We have explored also whether the variation of the PSF along the image can affect the recovery of the structural parameters. To do that we have made a conservative test reanalysing the full set of galaxies in the  $K_s$  band using a PSF with a FWHM  $2\sigma$  times larger than the value of the median FWHM of the PSFs. The results of doing this are shown in Fig. 4.

Only very compact galaxies with effective radii similar or smaller than the pixel size are significantly affected by the change of the PSF along the field of view. In those cases the estimation of the index  $n$  is pretty uncertain and we can not allocate these galaxies to the low- $n$  or high- $n$  categories. These objects amount to  $\sim 20\%$  of our sample. According to their SEDs these objects are not misidentified stars neither are they compatible with being at  $z < 1$ . Because of their extremely compact nature some of them could be AGNs. In fact, for the brightest object, MS1356, where spectroscopic analysis has been made (van Dokkum et al. 2003;2004) the AGN hypothesis is confirmed. In that case, their sizes could be not indicative of the sizes of their host galaxies. However, we can not assure the AGN nature for all these objects, so we have decided to explore how large could be the effect of these objects in our luminosity-size and stellar mass-size relations (see section 4.1 and 4.2).

For the rest of the sample ( $\sim 80\%$  of our objects) the estimation of the structural parameters is robust to changes in the selected PSF to analyze the data: the scatter between the sizes is  $\lesssim 14\%(1\sigma)$  and the scatter between the Sérsic index  $n$  is  $\lesssim 30\%(1\sigma)$ .

### 3.1.4. Size estimates at fixed $n$

Another possible test to estimate the robustness of our size estimations is to reanalyze the objects using this time the Sérsic index parameter fixed at  $n=1$  or  $n=4$ . We have repeated our analysis for the galaxies in the MS1054 field using the filters which match the V-band rest-frame at every  $z$ . All the galaxies are fitted initially with  $n$  fixed to 1 and then refitted using  $n$  equal to 4. From

these two fits we take that with the minimum  $\chi^2$  value as representative of the galaxy structural properties.

The comparison between the structural parameters recovered using  $n$  fixed and  $n$  free is shown in Fig. 5. Galaxies better fitted by an exponential profile ( $n=1$ ) have  $0 < n < 2$  when this parameter is left free during the fit. In addition, galaxies well fitted by a de Vaucouleurs profile ( $n=4$ ) yield  $n$  ranging from 1.5 to 7. It is interesting to note that there is some overlap between both regimes ( $1.5 < n < 2$ ). From the results presented here and in 3.1.1, it seems to be possible to discriminate between highly and less concentrated objects (i.e. those with  $n_{input}$  larger or smaller than 2.5 respectively) using  $n_{output}=1.5$  as the separation criterion. In fact, if we assume, as suggested by our simulations, up to a 50% bias on the index  $n$  for the high-concentrated objects, an object with original  $n_{input}=3-4$  would be identified in our code as  $n_{output}=1.5-2$ . It is important to note that our criterion for separating the galaxies using  $n_{output}=1.5$  would be similar to using  $n=2.5$  in a case where the index  $n$  was less biased than in the current analysis (see e.g. Barden et al. (2005)). In what follows, we will take advantage of this to facilitate a comparison of our results with those found at lower  $z$  (see Sections 4 and 5.1).

The sizes estimated using  $n$  fixed or  $n$  free during the fit show very good agreement with only  $\sim 7\%$  ( $1\sigma$ ) of relative scatter between them and no significant bias.

### 3.1.5. Comparison with NICMOS data

We have obtained deep H-band NICMOS images of the HDF-S. These NICMOS data consist of 8 pointings of camera 3 ( $52'' \times 52''$ ,  $0.203''/\text{pix}$ ). Each pointing is the combination of 6 sub-pixel dithered exposures, with a total exposure time of 1.5 hours. The final mosaic was assembled using the *drizzle* task and has a pixel scale of  $0.119''$  to match our ISAAC ground-based data<sup>14</sup>. A detailed presentation of this dataset and an analysis of the sizes of the galaxies in this image will be presented in Zirm et al. (2006).

We have 27 galaxies in common between ISAAC and NICMOS images in the redshift range  $1.5 < z < 2.6$  for which we analyze the H-band images. We found a good correlation between the sizes measured in the NICMOS images compared with those measured with ISAAC. The scatter is  $24\%(1\sigma)$  with no systematic bias between both measurements.

## 3.2. Selection Effects

In practice, any image presents a surface brightness limit beyond which the sample is incomplete. To characterize this limit is particularly important for high- $z$  samples where the effects of the cosmological surface brightness dimming are severe. For a given total flux limit, the surface brightness limit translates into an upper limit on the size for which a galaxy can be detected.

To determine the detection map of the FIRES MS1054  $K_s$ -band image we have created a set of  $10^5$  mock sources with intrinsic exponential profiles uniformly distributed as follows:  $K_s$ -band total magnitudes between 18 and 24 mag, effective radius  $r_e$  between 0.03 and 3 arcsec and inclination angles between 0 and 90 degrees. Readers

<sup>14</sup> The ISAAC pixel scale is actually  $0.''147$ ; however, we resampled the ISAAC pixels to  $3 \times 3$  blocked HDF-S WFPC2 pixels.

more interested in the simulations are referred to Förster Schreiber et al. (2006)<sup>15</sup>. The simulated sources are placed randomly on the real image 20 at a time and extracted as for the real source detection. On doing that we construct a detection map giving the number of recovered sources over the number of input artificial sources per input magnitude and input  $\log(r_e)$  bin (see Fig. 6a). A equivalent analysis for the HDF-S field is presented in Fig. 8 of Trujillo et al. (2004). It is important to note that in selecting exponential profiles ( $n=1$ ) for estimating our detection map we are being conservative from a detection standpoint. Galaxies with larger  $n$ , and consequently more centrally concentrated, would be much easier to detect at a given magnitude.

We have also estimated the completeness map (see Fig. 6b) of our survey for those galaxies with measured magnitude  $K_s < 23$ . To do that we have computed the ratio between the number of recovered sources with output magnitude and output size over the number of input sources within that magnitude and size bin. To estimate the output magnitudes and sizes we have used exactly the same tools as for actual galaxies. Overplotted on the completeness map is the distribution of the full sample of  $K_s$  band selected objects in the MS1054 field. Highlighted in this distribution are those objects which are used in this paper (i.e. those with  $1 < z < 3.2$ ).<sup>ste</sup>

As a second step to analyze the effect of completeness in our sample we have probed whether the size distribution of our objects could be affected by the completeness. In Fig. 6c we show the completeness for three different magnitude intervals:  $20 < K_s < 21$ ,  $21 < K_s < 22$  and  $22 < K_s < 23$  as a function of the size. In addition, we overplot the size distribution (arbitrarily normalized to have a value at the peak equal to the value of the completeness curve at that point) of real galaxies in the same intervals. The number of observed galaxies decreases more rapidly to larger sizes than do the completeness curves. This shows that incompleteness is not affecting the extent of our size distribution to larger sizes. A similar analysis but this time using only the faintest magnitude bin ( $22 < K_s < 23$ ) is done separating the galaxies according to their redshift (Fig. 6d). This figure shows that the size distribution of the observed galaxies in the magnitude interval  $22 < K_{s,input} < 23$  is not related with the redshift of the objects. Interestingly, Bouwens et al. (2004) show, using UDF images, that the principal effect of increased depth is to add galaxies at fainter magnitudes, not larger sizes, demonstrating that high- $z$  galaxies are predominantly compact and that large low surface brightness objects are rare. This result provides independent corroboration of our analysis. The effect of the completeness in the robustness of our relations is explored in Sec. 4.3.

The interested reader could also see how the size distribution of the SDSS galaxies would look like under the FIRES sample selection effects (Trujillo et al. 2004; their section 4.1). The depth of our images ensures that the largest SDSS galaxies would be detected if they were present in our sample.

We have also quantified the mass and luminosity limits implied by our observed magnitude limit. In doing so we

try to serve the dual purpose of maximizing the number of objects in our sample while simultaneously reducing systematic biases on the final results. We determine our rest-frame luminosity limit using the  $K_s$  magnitude and the expected color of an Scd template at  $z = 2.5$ , the center of our highest redshift bin. For  $K_s = 23.5$  this limit is  $L_V > 3.4 \times 10^{10} h_{70}^{-2} L_\odot$ . Above this limit we are complete at all redshifts  $z \lesssim 2.5$  in the HDF-S field. We adopt the same limit for the MS1054 data acknowledging that we will be missing galaxies in our higher redshift bin with  $23 < K_s < 23.5$ . As shown in Figs. 8 and 10, however, the distributions in size, luminosity, and mass of objects in the MS1054 and the HDF-S fields are similar and we make the assumption that this incompleteness in the highest redshift MS1054 data will not significantly bias our results.

We choose two separate means of defining a limit in mass. For our first mass limit we choose the lowest observed mass in our combined sample at  $z \sim 2.5$  (see Fig. 7). This limit is  $M_* > 3 \times 10^{10} h_{70}^{-2} M_\odot$ . We realize that only the objects with the lowest mass-to-light ratios will be detectable at these masses and that we are incomplete to objects of higher mass-to-light ratios. Nonetheless we use this limit to maximize the total number of objects in our sample, keeping in mind that we may experience systematic biases from our mass incompleteness. As a more conservative approach we also choose a mass limit corresponding to the maximum stellar mass-to-light ratio expected at  $z \sim 2.5$ . We use a maximally old single stellar population from Bruzual & Charlot (2003) with solar metallicity and a Salpeter (1955) IMF. At  $z \sim 2.5$  the Universe is  $\sim 2.6$  Gyr old for our cosmology and the resultant mass-to-light ratio is 1.93. Coupled with our luminosity limit of  $3.4 \times 10^{10} h_{70}^{-2} L_\odot$ , this yields a mass limit of  $M_* > 6.6 \times 10^{10} h_{70}^{-2} M_\odot$ . Above this limit we are complete to objects of every stellar mass-to-light ratio, although we have very few objects and our random errors will be large. The differences between results using these two limits are discussed in the end of § 6. As done for the luminosity threshold we adopt the limits for the HDF-S for the whole sample.

#### 4. THE OBSERVED LUMINOSITY/STELLAR MASS VS SIZE RELATIONS AT HIGH-Z

##### 4.1. Luminosity vs size

We now present the relation between luminosity and the rest-frame V-band size, covering the redshift range  $1 < z < 3.2$  for the HDF-S and the MS1054 fields. The low redshift limit is selected to avoid the influence of cluster galaxies at  $z=0.83$  in the MS1054 field and the high redshift limit is chosen to maintain our analysis of the high- $z$  galaxies in the optical rest-frame. We convert our measured angular sizes to physical sizes using the photometric redshift (or the spectroscopic value when available) determined for each object.

In Fig. 8 our sample is split in three different redshift bins:  $1 < z < 1.4$ ,  $1.4 < z < 2$  and  $2 < z < 3.2$ . This separation allows us to study the galaxies in roughly equal time intervals of  $\sim 1.2$  Gyr.

The top row shows the luminosity-size relation for the full sample. The middle row and the bottom row show the same relation but this time separating the galaxies by their concentration. For objects with  $r_e < 0.''125$  the

<sup>15</sup> Simulations shown in Förster Schreiber et al. (2006) only consider point sources with an input magnitude distribution following the slope of the counts.

estimation of the Sérsic index  $n$  is uncertain. To indicate this uncertainty these objects are plotted simultaneously in the low and high- $n$  rows using lighted symbols.

Overplotted on our observed distributions are the mean and dispersion of the distribution of the Sérsic half-light radii from the Sloan Digital Sky Survey (SDSS; York et al. 2000) galaxies. We use the “local” SDSS sample for reference. The sizes are determined from a Sérsic model fit (Blanton et al. 2003). The characteristics of the sample used here are detailed in Shen et al. (2003). The mean of the SDSS galaxies redshift distribution used for comparison is 0.1. We use the sizes and the shapes estimated in the observed  $r$ -band as this closely matches the  $V$ -band restframe filter at  $z \sim 0.1$ . The luminosity of the SDSS galaxies in the restframe  $V$ -band are estimated by interpolating between the restframe  $g$ -band and  $r$ -band luminosities (S. Shen, private communication).

In the first row, our sample is compared to the total population observed by SDSS, whereas in the second row we compare with the galaxies classified by Shen et al. as late-type and in the third row with those classified as early-type. Their early or late-type classification is based on the Sérsic index: galaxies with  $n < 2.5$  are considered late-types and galaxies with  $n > 2.5$  are identified as early-types. It is important to note that using even smaller index  $n$  values like  $n=2$  as the criterion for the separation between early- and late-type galaxies in the SDSS does not produce a significant change in the luminosity- and stellar mass-size relations (S. Shen, private communication). This is as expected because of the scatter between the Sérsic index  $n$  and the Hubble Type relation (see e.g. Fig. 1 of Ravindranath et al. 2004). Consequently, changing from  $n=2$  to  $n=2.5$  (or vice versa) does not change substantially the morphological type of the galaxies under study, and therefore, the effect on the luminosity-size or stellar mass-size relations is small.

Returning now to the redshift evolution, Fig. 8 shows that at a given luminosity, galaxies are progressively smaller at higher  $z$ . Of course, this evolution of the luminosity-size relation can be interpreted differently: at a given size, galaxies were more luminous at higher  $z$ .

To quantify the evolution of these relations as a function of redshift, we show in Fig. 9 the ratio between the observed size and the expected size (at a given luminosity) from the SDSS distribution versus  $z$ . To estimate the expected size from SDSS at a given luminosity we interpolate linearly between the SDSS points when necessary. From this plot the evolution in size (at a given luminosity) with  $z$  is evident. Galaxies with  $L_V \gtrsim 3.4 \times 10^{10} h_{70}^{-2} L_\odot$  at  $z \sim 2.5$  are  $\sim 3.5$  times smaller than for equally luminous galaxies today. In the second row of this figure we show the evolution of the mean and the dispersion (large error bars) of the above ratio estimated from the  $\ln(r_{e,c}/r_{e,SDSS})$  distribution. These quantities are estimated in the same redshift bins as stated above. The small error bars enclose the  $2\sigma$  uncertainty of the means. To evaluate these error bars we have used a bootstrapping method.

As in Fig. 8, those galaxies with  $r_e < 0.125$  are plotted with lighted symbols. To measure how much these small galaxies could affect the luminosity-size evolution we have made the most conservative approach we can do. First, we have assumed that all those galaxies are in the

low- $n$  bin and we have reestimated the mean value of the  $\log(r_{e,c}/r_{e,SDSS})$  distribution accounting for the contribution of the small galaxies. The range of variation of the mean is shown with the grey error bar. In a second step, we have assumed that all those galaxies belong to the high- $n$  bin and we have repeated the same exercise.

#### 4.2. Stellar mass vs size

We have also explored the relation between stellar mass and size for our sample (Fig. 10). The stellar mass-size distribution evolves less than the luminosity-size relation at high- $z$ . The stellar mass-size relation presents more scatter than the luminosity-size relation because the stellar mass is an indirectly inferred property. This scatter is ultimately related to the uncertainty in the M/L determinations for these galaxies. The evolution with redshift of the sizes of the galaxies at given stellar mass is illustrated in Fig. 11 where we show the ratio between the observed size and the expected size (at a given stellar mass) according to the SDSS local sample. The potential contribution of the small galaxies to this relation is estimated as for the luminosity-size relation.

The SDSS stellar masses used in Shen et al. (2003) are derived from stellar absorption line indices centered on the inner region of the galaxies whereas the present work uses colors integrated over the full galaxy. As discussed in Kauffmann et al. (2003) this difference in techniques is particularly important for brighter galaxies as they have strong color gradients, such that the central colors are not indicative of the luminosity weighted total colors. According to that work the mass-to-light ratio derived from line indices are biased to higher values than those measured from integrated colors. To avoid this problem, we have re-estimated the stellar masses of SDSS for this work using the restframe  $(g-r)$  color (S. Shen, private communication) and applying the transformation suggested for this color in Bell et al. (2003). This transformation is based on a Kroupa (2001) IMF. To match their values with the FIRES data (which uses a Salpeter IMF) we apply the transformation suggested in Kauffmann et al. (2003):  $M_{IMF,Salpeter} = 2 \times M_{IMF,Kroupa}$ .

#### 4.3. Robustness of the Luminosity-size and stellar mass-size estimates

The luminosity- and stellar mass-size relations presented in the previous sections are based on our direct measurements without making any attempt to correct for possible biases in the structural parameters as indicated by the simulations. To check whether the presented results are robust we have repeated our analysis correcting this time the observed structural parameters following the indications of our simulations (Table 2). In this particular case, the separation between low- $n$  and high- $n$  galaxies is done using  $n=2.5$  as the separation criterion. In addition, we have also repeated our analysis using the size estimation from the fits using  $n$  fixed. We summarize the results of these tests on Fig. 12.

As expected, due to the smaller sub-sample of galaxies and the larger corrections suggested by the simulations, the least robust results are for galaxies with the larger light concentration (high- $n$ ). However, it is interesting to note that all the estimates of the mean relation are in agreement within  $\sim 1\sigma$ . As most of our galaxies have a small index  $n$  value, the corrections are small for most

of the sample. Consequently, the relations using the corrections suggested by the simulations do not change our main results. In addition, when we compare our relations using  $n$  free with those obtained using  $n$  fixed to  $n=1$  or  $n=4$ , we do not observe systematic effects.

We have also studied whether the weak magnification lensing of the MS1054–03 foreground cluster can affect the result of our analysis. The cluster mass distribution has been modeled by Hoekstra, Franx & Kuijken (2000). The average background magnification effects over the field of view covered by FIRES observation range from a few % to 25% between  $z=1$  to 4. The magnification is most significant in the immediate vicinity of the cluster central region. The Einstein radius  $r_E$  of this cluster is estimated to be  $\sim 15$  arcsec. We have removed from our sample all the galaxies located within  $2r_E$  (this implies 9 objects). Outside this region the magnification is expected to be very small. The result of removing these galaxies in our relations is shown in Fig. 12. As expected from the small number of objects within  $2r_E$  the effect on our relations is very tiny.

Finally, we have explored the effect of the completeness in our relations. To do this we have weighted every galaxy of our sample with the inverse value provided by our completeness map at every magnitude and size bin. The relations obtained using the weights are shown in Fig. 12. As that figure shows, due to the high completeness of our sample, the observed relations remain basically unchanged. It should be noted, however, that our completeness map is strictly valid only under the assumption of an uniform input distribution with all the galaxies well described by an exponential profile. This assumption is realistic for  $\sim 65\%$  of our sample.

The above tests indicate that the results presented in this paper are robust. Because the main results of this paper are insensitive to the corrections, we perform our analysis based purely on the direct measurements. Applying these corrections artificially increases the scatter of our relations because of the necessary approximations when correcting. We find that the increase of the scatter is  $\sim 20\text{--}40\%$  in the corrected distributions related to those based on the direct estimations.

#### 4.4. Robustness of the local SDSS relations

Our analysis of the evolution of the luminosity–size and stellar mass–size relations with redshift depends on the accuracy of the Shen et al. (2003) SDSS local relations. Driver et al. (2005) have pointed out, using the Millennium Galaxy Catalog (MGC), that surface brightness selection could bias the Shen et al. results. Driver et al. (their Fig. 19) show an uniform offset of  $\delta\mu^e \sim 0.4$  mag arcsec $^{-2}$  in the luminosity–surface brightness distributions between their estimations and the Shen et al. relations. At a given luminosity, the global distribution of galaxies in the Shen et al. data presents a mean surface brightness  $\sim 0.4$  mag arcsec $^{-2}$  brighter than in the Driver et al. work. If we translate this into effective radii this would imply that Shen et al. mean effective radius estimations are (at a given luminosity) a factor  $10^{-0.2\delta\mu^e}$  (i.e.  $\sim 0.83$ ) smaller than the Driver et al. values. To account (crudely) for this offset in our size evolution estimations we would need to multiply the values presented in Table 5 by the above factor. In this sense, the evolution reported in this paper would be slightly less strong

( $<20\%$ ) than the evolution estimated using the MGC data as a reference. In any case, it is worth noting that the main results of our papers would be basically unchanged by this potential offset.

Similarly, we have also estimated the mean offset in size at a given luminosity between the very low redshift ( $z < 0.05$ ) SDSS sample from Blanton et al. (2005) and the Shen et al. relations. We have done this for brightest population ( $L_V \gtrsim 3.4 \times 10^{10} h_{70}^{-2} L_\odot$ ). For these galaxies we found  $\langle \text{re}_{Shen} / \text{re}_{Blanton} \rangle = 0.86$ . This value is similar to that reported above comparing with the MGC galaxies, however, in this case the difference must be taken with caution as it could be slightly affected by potential evolution of the mean size of the galaxies since  $z \sim 0.1$  (Shen et al.) to  $z \sim 0$  (Blanton et al.).

## 5. ANALYSIS

### 5.1. Comparison of FIRES data to the evolution at $z < 1$

Several analyses of the luminosity–size evolution of galaxies in the optical rest–frame up to  $z \sim 1$  have been carried out (Im et al. 1996; 2002, Lilly et al. 1998, Schade et al. 1999, Simard et al. 1999, Ravidranath et al. 2004; Trujillo & Aguerrí 2004; McIntosh et al. 2005; Barden et al. 2005). These studies seem to agree on a moderate decrease of the surface brightness of the galaxies towards the present:  $<1$  mag in the V–band restframe (or equivalently an increase in size at a given luminosity of  $\lesssim 35\%$ ).

In order to make a consistent comparison at lower redshifts with FIRES, we use the data from the largest sample currently available at intermediate redshift: the GEMS survey (Rix et al. 2004). GEMS is a large-area (800 arcmin $^2$ ) two-color (F606W and F850LP) imaging survey with the ACS on the HST to a depth of  $m_{AB}(F606W) = 28.3(5\sigma)$  and  $m_{AB}(F850LP) = 27.1(5\sigma)$  for compact sources. Focusing on the redshift range  $0.2 \leq z \leq 1$ , GEMS provides morphologies and structural parameters for nearly 10,000 galaxies for which redshift estimates, luminosities, and SEDs exist from COMBO-17 (Classifying Objects by Medium–Band Observations in 17 Filters; Wolf et al 2001, 2003).

The luminosity–size and stellar mass–size relations of this survey are presented in Barden et al. (2005; late–type galaxies) and McIntosh et al. (2005; early–type galaxies). The GEMS late– and early–type separation criteria is based on the Sérsic index  $n$ . Late–types are defined through  $n < 2.5$ , and early–types through  $n > 2.5$  and a color within the “red–sequence” (Bell et al. 2004). We have checked that adopting smaller index  $n$  values like  $n=2$  instead of  $n=2.5$  as the separation criterion does not produce a significant change in their results. The stellar masses of the GEMS survey used in the present work are derived in the same way as those in FIRES<sup>16</sup>. Using their measurements of size, luminosity, mass, redshift and completeness we have repeated the same analysis as for the FIRES sample. To ensure homogeneity with the FIRES sample we have only selected GEMS galaxies with  $L_V > 3.4 \times 10^{10} h_{70}^{-2} L_\odot$  (in the case of the luminosity–size relation) and  $M_\star \gtrsim 3 \times 10^{10} h_{70}^{-2} M_\odot$  (in

<sup>16</sup> In Barden et al. (2005) and McIntosh et al. (2005) the GEMS stellar masses are also estimated from stellar populations models, finding no differences in the resulting stellar mass–size relation.



the case of the stellar mass–size relation). The resulting size evolution from both surveys together are shown in Fig. 13 and Table 5.

From this comparison we see that the  $z < 1$  evolution (GEMS) and  $z > 1$  evolution (FIRES) derived from two independent analyses and data sets match well. We discuss this in more detail in Sect. 6.

### 5.2. Comparison of FIRES to other works at $z > 1$

Papovich et al. (2005) have measured the evolution of the sizes in the B–band restframe for galaxies in the HDF–N using WFPC2 and NICMOS imaging. Papovich et al. measured sizes using SExtractor and not accounting for the PSF effect in their measurements. At  $z \sim 2.3$  they find a mean value of  $2.3 \pm 0.3$  kpc for  $M(B) \leq -20.0$ . For galaxies with  $M(V) \leq -21.5$  at  $z \sim 2.5$  we have  $2.0 \pm 0.2$  kpc. In both cases the error represents the uncertainty on the mean. The agreement is encouraging taking into account the different image quality and methods used for retrieving the half–light radii.

At even larger redshifts, analysis of  $1 < z < 6$  galaxies based on the optical bands (and consequently, matching the UV rest–frame) show a strong decrease in size at a given UV luminosity with increasing redshift. This decrease scales with  $z$  as:  $(1+z)^{-1.5}$  (Ferguson et al. 2004) or as  $(1+z)^{-1}$  (Bouwens et al. 2004). In agreement with these results, in the redshift range  $1 < z < 3$  the sizes at a given V–band luminosity presented here are well described by  $(1+z)^{-0.8 \pm 0.3}$ . Consequently, the shape of the evolution is similar in the UV and in the V–band restframe at least in the above redshift range.

### 5.3. Comparison with previous HDF–S FIRES results

Trujillo et al. (2004) explored the size evolution of the galaxies contained in the HDF–S. Their results are summarized in their Table 2. It is interesting to check whether our current results, obtained with a larger sample, agree with this previous analysis. At  $z \sim 2.5$ , for galaxies more luminous than  $2 \times 10^{10} h_{70}^{-2} L_{\odot}$  they found that sizes were  $\sim 3 \pm 1$  ( $\pm 1 \sigma$ ) times smaller than today counterparts. For galaxies more massive than  $2 \times 10^{10} h_{70}^{-2} M_{\odot}$ , sizes were  $\sim 1.4 \pm 0.5$  ( $\pm 1 \sigma$ ) times smaller than local galaxies of the same stellar mass.

For our current full data set, at  $z \sim 2.5$ , galaxies more luminous than  $3 \times 10^{10} h_{70}^{-2} L_{\odot}$  are  $3.8 \pm 0.5$  ( $\pm 2 \sigma$ ) smaller, and galaxies more massive than  $3 \times 10^{10} h_{70}^{-2} M_{\odot}$  are  $2.1 \pm 0.3$  ( $\pm 2 \sigma$ ) smaller than same objects today. These values are larger than those obtained in the HDF–S subsample but are consistent within the uncertainties.

### 5.4. Analytical description of the size evolution

To provide an analytical description of the rest–frame size evolution of the galaxies in the redshift range  $0 < z < 3$ , we have fitted the observed size evolution at a given luminosity ( $L_V \gtrsim 3.4 \times 10^{10} h_{70}^{-2} L_{\odot}$ ) and at a given stellar mass ( $M_{*} \gtrsim 3 \times 10^{10} h_{70}^{-2} M_{\odot}$ ) to two different analytical functions: a)  $(1+z)^{\alpha}$  and b)  $H^{\alpha}(z)$ . The parameters of the fits are obtained by minimizing the  $\chi^2$  error statistic. To avoid confusion with lines drawn from comparison with theoretical models we do not overplot these fits in Fig. 13. The results of our fits, however, are shown in Table 6. In the low– $n$  case a better fit is obtained using the function  $H^{\alpha}(z)$ .

### 5.5. Opacity effect on attenuation and size measurements

The estimation of the brightness and the size of the galaxies is affected by the dust content. Using the model of Popescu et al. (2000), the effect of dust on the luminosity (Tuffs et al. 2004) and on the scalelength measurement (Möllenhoff et al. 2006; in preparation) has been quantified: a larger amount of dust increases the attenuation and the observed size (in terms of scalelength) of the objects. The observed size is larger because the dust is more strongly concentrated towards the central region of the galaxies and consequently the flux gradient is flattened.

The size evolution presented in this paper is measured in relation to the observed (uncorrected for dust) size of the local galaxies, consequently if the dust opacity were not to change with redshift the observed evolution presented in this paper would remain unchanged. However, it is likely that the opacity of the galaxies changes with redshift.

At a fixed inclination, bulge–to–total ratio and restframe wavelength, the degree of attenuation and the increase in the observed scalelength due to dust can be parametrized by the change in the central face–on optical depth. The optical depth is a very uncertain quantity (even in the nearby universe) and this makes a detailed evaluation of the effect of dust beyond the scope of this paper. Consequently, we have not made any attempt to correct our results for the effect of opacity. Nevertheless, in order to provide a crude estimation of how a significant increase in opacity could affect our results we have made the following exercise: let’s assume a mean inclination of  $30^{\circ}$  and a increase in the total central face–on optical depth in B–band from 4 (present–day galaxies) to 8 (high– $z$  galaxies). This change implies a transition from an intermediate to a moderately optically thick case. In this case, for a disk–like galaxy observed in the V–band restframe, the attenuation increases by  $\sim 0.2$  mag (Tuffs et al. 2004; their Fig. 3 and Table 4) and the scalelength increases by  $\sim 15\%$  (Möllenhoff et al. 2006; in preparation). If we account for these numbers, the galaxies in our high– $z$  sample would be intrinsically brighter by  $\sim 20\%$  and intrinsically smaller by  $\sim 15\%$ . In this sense, the observed (uncorrected for dust) size evolution presented in this paper would be a lower limit of the actual size evolution. If the opacity were smaller in the past then the situation would be reversed, with our current estimation of the size evolution being an upper limit.

## 6. DISCUSSION

We have greatly expanded the FIRES sample of galaxy rest–frame optical size measurements, compared to Trujillo et al. (2004), and have combined these with data from GEMS and SDSS. This combined data set allows us to analyze the evolution of the luminosity–size and the stellar mass–size relations for luminous ( $L_V \gtrsim 3.4 \times 10^{10} h_{70}^{-2} L_{\odot}$ ) and massive ( $M_{*} \gtrsim 3 \times 10^{10} h_{70}^{-2} M_{\odot}$ ) galaxies over 80% of the Universe’s age ( $0 < z < 3$ ). During that time their luminosity–size relation has changed strongly but the stellar mass–size relation has evolved less than the luminosity–size relation. As suggested in Trujillo et al. (2004) these two results can be reconciled when we take into account the strong mass–to–light ratio evolu-

tion that galaxies have experienced in the past. Such M/L evolution must also play a big role in explaining the strong  $L_{UV} - r_{e,UV}$  evolution seen in high- $z$  samples (e.g. Ferguson et al. 2003).

Beyond the empirical result, it is of interest to compare the observed evolution with the theoretical predictions. In Fig. 13 we show the expectations from semianalytical hierarchical and infall models for disk-like galaxies compared to the observed size evolution. We first concentrate our attention on the evolution of the sizes at a given luminosity. The semi-analytic hierarchical Mo et al. (1998) model makes predictions on the disk size evolution at a given halo mass or circular velocity, assuming that the disk mass is a fixed fraction of the halo mass. If one then identifies Mo et al. disk mass with the stellar mass, or even the stellar luminosity (as done e.g. by Ferguson et al. 2003) then a size-luminosity scaling of  $H^{-2/3}(z)$  results. This scaling is shown in the top left panel of Fig. 13, tantalizingly following the observations (except for the last point at  $z=2.5$ ). Yet, it must be borne in mind that this match implies a mean stellar M/L that is constant with redshift, known to be incompatible with the color evolution of the same galaxies. The agreement between  $H^{-2/3}(z)$  and the data must therefore be considered fortuitous, rather than a direct confirmation of the Mo et al. model.

The infall (Bouwens & Silk 2002) model predicts directly the evolution of the size at a given luminosity for Milky Way type objects. For that reason, we compare the infall model only with the observed size evolution at a given luminosity for galaxies with exponential-type profiles (upper left panel in Fig. 13). We see that the agreement of this model with the observed evolution is excellent for galaxies at all  $z$ . The infall model, however, must fail at higher  $z$ . In fact, this model shows an improbably fast decrease for galaxies with  $z > 2.5$  and, for  $z \gtrsim 3.7$ , this model produces sizes with values less than zero.

If we focus now on the size evolution at a given disk mass and assume that the stellar mass is a good indicator of the total baryonic mass settled in the disk (which the gas fraction at high redshift might invalidate), we can make a comparison between the Mo et al. model prediction and the observed size evolution at a given disk mass. The bottom left panel of Fig.13 shows that this hierarchical model (under the assumption stated in the Introduction) produces a stronger evolution in the sizes than is observed. However, at all  $z$  the model can not be rejected at  $3\sigma$  confidence level. Consequently, although the observed evolution is weaker than the predicted size evolution  $R \propto H^{-2/3}(z)$  at a fixed halo mass, this model can not be rejected with the present dataset.

The Mo et al. (1998) model describes the evolution of the baryonic disk size at a given halo mass whereas the data show the stellar disk size evolution at a given stellar mass. We now explore whether this difference maybe responsible for the data model discrepancy apparent in the bottom left panel of Fig.13. We consider two aspects: a) the ratio of the stellar mass to the halo mass,  $M_*/M_{halo}$ , can evolve with redshift and b) the ratio of the stellar disk to the baryonic disk size,  $R_*/R_{disk}$ , can also change.

These factors can be visualized by writing out the fol-

lowing identity:

$$\frac{R_*}{M_*^{1/3}}(z) = \frac{R_{disk}}{M_{halo}^{1/3}}(z) \times \left( \frac{M_{halo}}{M_*}(z) \right)^{1/3} \times \frac{R_*}{R_{disk}}(z) \quad (2)$$

where  $R_*/M_*^{1/3}$  are the observables and  $R_{disk}/M_{halo}^{1/3}$  are the quantities more immediately predicted by Mo et al. (1998).

One possible choice to describe the accumulation of stellar mass within halos is by the globally measured build-up of stellar mass:  $M_*/M_{halo}(z) \sim \langle \rho_*(z) \rangle$ , where we take  $\langle \rho_*(z) \rangle$  from Rudnick et al. (2003). Taking  $R_*/R_{disk} \equiv 1$  for now, this picture would predict a nearly redshift-independent  $R_* - M_*$  relation (dotted line in bottom left panel of Fig. 13). However, this picture would imply that stellar disks form from early-on in large halos and that the stellar disk, already in its infancy ( $M_*/M_{halo} \ll M_*/M_{halo}(z=0)$ ) samples the full angular momentum distribution of its large halo.

From a variety of observational and theoretical arguments  $R_*/R_{disk}$  cannot be unity at all epochs. As the solid line in Fig. 13 illustrates, through altering this assumption by 15–30% (i.e. by assuming  $R_*/R_{disk}(z) \propto H^{-1/5}(z)$ ) it would be easy to match the observations.

The degree of evolution in the observed stellar mass-size relation with redshift implies that galaxies must evolve with time, increasing their size as they build up their stellar mass. Consequently, galaxies on average appear to grow inside-out. Newly formed stars must preferentially reside at larger and larger radii (Trujillo & Pohlen 2005).

In interpreting the evolution of spheroid-like objects a different reference hypothesis suggests itself: we analyze whether the decrease in typical galaxy effective radius with lookback time at a given luminosity is consistent with a passively fading galaxy population.

To test the above idea we plot on Fig. 13 different tracks showing the expected size evolution of a fading galaxy population with different formation redshifts. These tracks are evaluated under the assumption that the shape of the local luminosity-size relation does not change with redshift but for a shift of the relation to brighter luminosities at increasing  $z$ . The increase in the luminosity with  $z$  is estimated by using the expected luminosity evolution from a single burst at high- $z$  (in our case, we have used  $z_{form} = 3, 5$  and  $7$ ) using the PÉGASE code (Fioc & Rocca-Volmerange 1997). Following the same procedure as with actual data, after shifting the luminosity-size relation we measure the ratio between the effective radii at a given luminosity for luminosities brighter than  $3.4 \times 10^{10} h_{70}^{-2} L_{\odot}$ . From the comparison, we see that the evolution of the luminosity-size relation for high- $n$  galaxies is consistent with a fading population of galaxies formed since  $z \sim 3$  to  $7$ .

However, although the above agreement is encouraging, the full population of spheroid galaxies we see today is unlikely to be evolving passively since  $z \sim 3$ . The passive scenario is against the observed evolution of the comoving total stellar mass density in passive red-sequence galaxies. This density is lower at earlier epochs, amounting to a factor of  $\sim 2$  buildup since  $z \sim 1$  (Chen et al. 2003; Bell et al. 2004; Cross et al. 2004) or a factor of  $\sim 10$  since  $z \sim 3$  (Labbé et al. 2005). This change can not be understood within a pure passive evolution scheme and

it is in agreement with the merger scenario proposed by Kauffmann & Haehnelt (2000). In addition, Daddi et al. (2005) find 4 very compact ( $r_e \lesssim 1$  kpc) and massive ( $M_* \gtrsim 10^{11} h_{70}^{-2} M_\odot$ ) objects at  $z \sim 1.7$  in the UDF. These objects could be the same class of compact galaxies that we find here and could be found it at redshift as low as  $z \sim 1$  (see Fig. 9 from McIntosh et al. 2005). In a  $\Lambda$ -CDM universe, Khochfar & Silk (2006a) find that early-type galaxies at high redshifts merge from progenitors that have more cold gas available than their counter parts at low redshift. As a consequence they claim that the remnant should be smaller in size at high redshift (Khochfar & Silk 2006b). These high- $z$  spheroid-like objects are very massive so it is not expected that their masses can increase dramatically since then. So, we must expect a mechanism of growing in size very rapidly at increasing their masses. As stated in the Introduction, the merger of early-type galaxies could increase their sizes. If this is the case, repeated mergers of the most massive spheroid-like objects that we observe at  $z > 1.5$  could bring them into the local observed stellar mass-size relation of early-type galaxies. A more detailed analysis of the nature of these compact objects in the FIRES sample will be presented in Toft et al. (2006) and Zirm et al. (2006).

We want to add a final cautionary note on the interpretation of the evolution of the luminosity-size and stellar mass-size relations. There is a hint that the degree of evolution of these relations could be different depending of the luminosity and stellar mass range (or size) analyzed (Barden et al. 2005; McIntosh et al. 2005). To test this we show in Fig. 14 the size evolution for galaxies more massive than our completeness mass limit ( $M_* \gtrsim 6.6 \times 10^{10} h_{70}^{-2} M_\odot$ ). In this case, the evolution in the sizes (at a given stellar mass) seems to be larger than if we maintain the current limit. However, the uncertainty particularly at the high- $n$  sample is very large to make any strong conclusion.

## 7. SUMMARY

Using very deep near-infrared images of the HDF-S and the MS1054-03 field from the FIRES survey we have analyzed the evolution of the luminosity-size and stellar mass-size relation, measured in their optical rest-frame, for luminous ( $L_V \gtrsim 3.4 \times 10^{10} h_{70}^{-2} L_\odot$ ) and massive ( $M_* \gtrsim 3 \times 10^{10} h_{70}^{-2} M_\odot$ ) galaxies with  $z > 1$ . By combining HDF-S with the MS1054-03 field we have tripled the number of galaxies with  $z > 1$  used in Trujillo et al. (2004).

Several tests have been run in order to estimate the robustness of our structural parameter estimates. From these tests we estimate an uncertainty in our sizes of  $\sim 25\%$  and in the concentration (Sérsic index  $n$ ) parameter of  $\sim 60\%$ . Moreover, we have briefly investigated whether our sample is affected by surface brightness selection effects. As shown in that cursory analysis, our magnitude selection criterion appear sufficiently conservative enough to avoid such a concern.

Combining the analysis of FIRES data with the results obtained by GEMS at  $z < 1$  (Barden et al. 2005; McIntosh et al. 2005) and tying both to the present-day results from SDSS (Shen et al. 2003) we trace a detailed picture of the evolution of the luminosity and stellar mass-size relations in the last  $\sim 11$  Gyrs. For less concentrated (low- $n$ ) objects, at a given luminosity, the

typical sizes of the galaxies were  $\sim 3$  smaller at  $z \sim 2.5$  than those we see today. In contrast, the stellar mass-size relation has evolved less: we see very little evolution to  $z \sim 1.2$  and a factor of  $\sim 2$  decrease in size at a given stellar mass at  $z \sim 2.5$ . The evolution at a given stellar mass has evolved proportional to  $(1+z)^{-0.40 \pm 0.06}$ . As pointed out by Trujillo et al. (2004) the different evolution in the luminosity-size and the stellar mass-size relation is explained by the fact that the M/L ratios of high- $z$  galaxies are lower than nowadays (or, the stellar populations were much younger at earlier times). The evolution observed in the stellar mass-size relation combined with the fact that galaxies are producing new stars implies an inside-out growth of the galactic mass.

The observed luminosity-size relation evolution out to  $z \sim 2.5$  for low- $n$  objects matches very well the expected evolution for Milky-Way type objects from infall models. For disk-like galaxies, the semi-analytical hierarchical predictions based on simple scaling relations between halos and baryons seem to overestimate the observed evolution of the stellar mass-size relation. The discrepancy is in the sense that the observed galaxies at high redshift are larger than expected from the model scalings. However, this model can not be totally rejected with the current dataset.

For highly concentrated (high- $n$ ) objects, the evolution of the luminosity-size relation is consistent with (but does not necessarily imply) pure luminosity evolution of a fading galaxy population. The evolution of the sizes at a given stellar mass is proportional to  $(1+z)^{-0.45 \pm 0.10}$ .

We are happy to thank Shiyin Shen for providing us with the Sloan Digital Sky Survey data used in this paper, E. F. Bell, E. Daddi and C. Heymans for useful discussions. We would like to thank C. Moellenhoff, C.C. Popescu and R.J. Tuffs for providing results from their calculations on the effects of dust on measured scale-lengths, prior to publication. We thank the staff at ESO for the assistance in obtaining the FIRES data and the Lorentz Center for its hospitality and support. We thank the anonymous referee for the detailed revision of our paper. Her/his comments have helped to improve the quality of the manuscript.

Funding for the creation and distribution of the SDSS Archive has been provided by the Alfred P. Sloan Foundation, the Participating Institutions, the National Aeronautics and Space Administration, the National Science Foundation, the US Department of Energy, the Japanese Monbukagakusho, and the Max-Planck Society. The SDSS Web site is <http://www.sdss.org>. The SDSS is managed by the Astrophysical Research Consortium (ARC) for the Participating Institutions. The Participating Institutions are the University of Chicago, Fermilab, the Institute for Advanced Study, the Japan Participation Group, Johns Hopkins University, Los Alamos National Laboratory, the Max-Planck-Institut für Astronomie (MPIA), the Max-Planck-Institut für Astrophysik (MPA), New Mexico State University, University of Pittsburgh, Princeton University, the US Naval Observatory, and the University of Washington.

GR acknowledges the support of a Goldberg fellowship at the National Optical Astronomy Observatory (NOAO), which is operated by the Association of Uni-

versities for Research in Astronomy (AURA), Inc., under a cooperative agreement with the National Science Foundation. GR also acknowledges the financial support of the Sonderforschungsbereich 375 Astroteilchenphysik. MB acknowledges support from the *Verbundforschung* of

the BMBF. DHM acknowledges support from the National Aeronautics and Space Administration (NASA) under LTSA Grant NAG5-13102 issued through the Office of Space Science.

## REFERENCES

- Barden, M. et al. 2005, ApJ, 635, 959  
 Blanton, M. R. et al., 2003, ApJ, 592, 819  
 Blanton, M. R., Lupton, R. H., Schlegel D.J., Strauss, M.A., Brinkmann J., Fukugita M., Loveday J., 2005, ApJ, 631, 208  
 Bell, E. F. & de Jong, R. S., 2001, ApJ, 550, 212  
 Bell, E. F., McIntosh, D.H., Katz, N., & Weinberg, M.D., 2003, ApJS, 149, 289  
 Bell, E. F. et al., 2004, ApJ, 608, 752  
 Bell, E. F. et al., 2006, ApJ, 640, 241  
 Bertin, E., & Arnouts, S., 1996, A&AS, 117, 393  
 Boehm, A., & Ziegler, B. L., 2006, astro-ph/0601505  
 Boylan-Kolchin, M., Ma C.-P. & Quataert, E., 2006, astro-ph/0601400  
 Bouwens, R. J., Cayón, L., & Silk, J. 1997, ApJ, 489, L21  
 Bouwens, R. J. & Silk, J. 2002, ApJ, 568, 522  
 Bouwens, R. J., Illingworth, G.D., Blakeslee, J. P., Broadhurst, T.J. & Franx, M., 2004, ApJ, 611, L1  
 Brook, C. B., Kawata, D., Martel, H., Gibson, B. K., Bailin, J., 2006, ApJ, 639, 126  
 Bruzual, G. & Charlot, S., 2003, MNRAS, 344, 1000  
 Casertano, S., Ratnatunga, K. U., Griffiths, R. E., Im, M., Neuschaefer, L. W., Ostrander, E. J. & Windhorst, R. A., 1995, ApJ, 453, 599  
 Casertano, S. et al. 2000, AJ, 122, 2205  
 Cayón, L., Silk, J. & Charlot, S. 1996, ApJ, 467, L53  
 Chen, H., et al. 2003, ApJ, 586, 745  
 Chiosi, C. & Carraro, G., 2002, MNRAS, 335, 335  
 Cole, S., Lacey C.G., Baugh, C. M. & Frenk C. S., 2000, MNRAS, 319, 168  
 Cross, N.J.G., et al., 2004, AJ, 128, 1990  
 Daddi, E., Cimatti, A., Renzini, A., Fontana, A., Mignoli, M., Pozzetti, L., Tozzi, P. & Zamorani, G., 2004, ApJ, 617, 746  
 Daddi, E. et al., 2005, ApJ, 626, 680  
 Dalcanton, J.J., Spergel, D. N., & Summers, F. J. 1997, ApJ, 482, 659  
 Driver, S. P., Liske, J., Cross, N.J.G., De Propis, R., & Allen P.D., 2005, MNRAS, 360, 81  
 Erb, D. K., Steidel C. C., Shapley, A. E., Pettini, M., Reddy N. A. & Adelberger, K. L., 2006, astro-ph/0604041  
 Eggen, O. J., Lynden-Bell, D., & Sandage, A. R., 1962, ApJ, 136, 748  
 Fall, S. M. & Efstathiou, G., 1980, MNRAS, 193, 189  
 Fall, S. M., 1983, in Athanassoula E., ed., Proc. IAU Symp. 100, Internal Kinematics and Dynamics of Galaxies. Reidel, Dordrecht, p. 391  
 Fasano, G. & Franceschini, A., 1987, MNRAS, 225, 155  
 Ferguson et al. 2004, ApJ, 600, L107  
 Floc, M., & Rocca-Volmerange, B., 1997, A&A, 326, 950  
 Förster Schreiber, N. M. et al. 2004, ApJ, 616, 40  
 Förster Schreiber, N. M. et al. 2006, AJ, 131, 1891  
 Franx, M. et al., "FIRES at the VLT: the Faint Infrared Extragalactic Survey", The Messenger 99, pp. 20–22, 2000  
 Franx, M. et al., 2003, ApJL, 587, L79  
 Giavalisco, M., Steidel C.C. & Macchetto, F.D., 1996, ApJ, 470, 189  
 Giavalisco, M., 2002, ARA&A, 40, 579  
 Graham, A. W. & Driver, S. P., 2005, PASA, 22, 118  
 Hoekstra, H., Franx, M. & Kuijken, K., 2000, ApJ, 532, 88  
 Im M., Griffiths, R.E., Ratnatunga, K.U., & Sarajedini V.L. 1996, ApJ, 461, L79  
 Im M. et al., 2002, ApJ, 571, 136  
 Kauffmann, G., & Charlot, S., ApJ, 430, L97  
 Kauffmann, G., & Haehnelt, M., 2000, MNRAS, 311, 576  
 Kauffmann, G., et al., 2003, MNRAS, 341, 33  
 Khochfar, S. & Burkert, A., 2003, ApJ, 597, L117  
 Khochfar, S. & Silk, J., 2006a, MNRAS, in press, astro-ph/0509375  
 Khochfar, S. & Silk, J., 2006b, ApJ, submitted  
 Kron, R. G. 1980, ApJS, 43, 305  
 Kroupa, P., 2001, MNRAS, 322, 231  
 Lacey, C., Guiderdoni, B., Rocca-Volmerange, B. & Silk, J. 1993, ApJ, 402, 15  
 Labbé, I.F.L. et al., 2003, AJ, 125, 1107  
 Labbé, I.F.L. et al., 2003b, ApJ, 591, L95  
 Labbé, I.F.L. et al., 2005, ApJ, 624, L81  
 Larson, R., 1975, MNRAS, 173, 671  
 Lilly, S. et al. 1998, ApJ, 500, 75  
 Lowenthal, J.D., Koo, D.C., Guzmán, R., Gallego, J., Phillips, A.C., Faber, S.M., Vogt, N.P., Illingworth G.D., 1997, ApJ, 481, 67  
 McIntosh, D. H., et al. 2005, ApJ, 632, 191  
 Merlin, E. & Chiosi, C., 2006, astro-ph/0605052  
 Mo, H. J., Mao, S. & White, S.D.M., 1999, MNRAS, 304, 175  
 Möllenhoff, C., Popescu, C.C. & Tuffs, R.J., 2006, in preparation  
 Moorwood, A. F. 1997, Proc. SPIE, 2871, 1146  
 Naab, T, Khochfar, S., & Burkert, A., ApJ, 636, L81  
 Naab, T, & Ostriker, J., 2006, MNRAS, 366, 899  
 Navarro, J., & Steinmetz, M. 2000, ApJ, 538, 477  
 Papovich, C., Dickinson, M., Giavalisco, M., Conselice, C.J. & Ferguson, H., 2005, ApJ, 631, 101  
 Peng, C.Y., Ho, L.C., Impey, C.D. & Rix, H.W., 2002, AJ, 124, 266  
 Press, W.H., Teukolsky, S.A., Vetterling, W.T. & Flannery, B.P., 1992, Numerical Recipes (Cambridge: Cambridge Univ. Press)  
 Popescu, C. C., Misiriotis, A., Kylafis, N. D., Tuffs, R. J., & Fischera, J. 2000, A&A, 362, 138  
 Ravindranath, S. et al. 2004, ApJ, 604, L9  
 Rix, H.-W. et al., 2004, ApJS, 152, 163  
 Roche, N., Ratnatunga, K., Griffiths, R. E., Im, M. & Naim, A., 1998, MNRAS, 293, 157  
 Rudnick, G. et al., 2001, AJ, 122, 2205  
 Rudnick, G. et al., 2003, ApJ, 599, 847  
 Rudnick, G. et al., 2006, ApJ, submitted  
 Salpeter, E.E., 1955, ApJ, 121, 161  
 Schade, D., Lilly, S.J., Le Fevre, O., Hammer, G. & Crampton, D., 1996, ApJ, 464, 79  
 Schade D. et al. 1999, ApJ, 525, 31  
 Sérsic, J.-L. 1968, Atlas de Galaxias Australes (Cordoba: Observatorio Astronomico)  
 Shen, S., Mo, H.J., White, S.D.M., Blanton, M.R., Kauffmann, G., Voges, W., Brinkmann, J. & Csabai, I., MNRAS, 2003, 343, 978  
 Smail, I., Hogg, D. W., Yan, L, Cohen, J. G., 1995, ApJ, 449, L105  
 Simard, L., 1998, Astronomical Data Analysis Software and Systems VII, A.S.P. Conference Series, Vol. 145, 1998, R. Albrecht, R.N. Hook and H.A. Bushouse, eds., p.108  
 Simard, L., et al. 1999, ApJ, 519, 563  
 Somerville, R. S., Primack, J. R., 1999, MNRAS, 310, 1087  
 Steidel C.C., Giavalisco, M., Pettini, M., Dickinson, M., & Adelberger, K. L., 1996, ApJ, 462, L17  
 Toft, S., et al. 2006, in preparation  
 Tran, K.-V. H., van Dokkum, P., Franx, M., Illingworth, G. D., Kelson, D. D. & Förster Schreiber, N. M., 2005, ApJ, 627, L25  
 Trujillo, I. et al., 2004, ApJ, 604, 521  
 Trujillo, I. & Aguerrri, J. A. L., 2004, MNRAS, 355, 82  
 Trujillo, I. & Pohlen, M., 2005, ApJ, 630, L17  
 Tuffs, R. J., Popescu, C. C., Völk, H. J., Kylafis, N. D. & Dopita, M. A. 2004, A&A, 419, 821  
 van den Bosch, F. C., 2000, ApJ, 530, 177  
 van Dokkum, P.G., Franx, M., Fabricant, D., Illingworth, G.D., & Kelson, D.D., 2000, ApJ, 541, 95  
 van Dokkum, P.G. & Franx, M., 2001, ApJ, 553, 90  
 van Dokkum, P.G. et al. 2003, ApJ, 587, L53  
 van Dokkum, P.G. et al. 2004, ApJ, 611, 703  
 van Dokkum, P.G., AJ, 130, 2647  
 Vogt N. P., Forbes, D. A., Phillips, A. C., Gronwall, C., Faber, S. M., Illingworth, G. D., Koo, D. C., 1996, ApJ, 465, L15  
 Vogt N. P. et al. 1997, 1997, ApJ, 479, L121  
 White, S.D.M, Frenk, C. S., 1991, 379, 52  
 Wolf C. et al., 2001, A&A, 365, 681  
 Wolf C., Meisenheimer, K., Rix, H.W., Borch, A., Dye, S., Kleinheinrich, M., 2003, A&A, 401, 73  
 York D. et al., 2000, AJ, 120, 1579  
 Zirm A. et al., 2006, in preparation

TABLE 1  
MOFFAT PSF FIT TO THE SAMPLE  
IMAGES

Filter	$\beta$	FWHM
HDF-S		
J <sub>s</sub>	3	0".46
H	3	0".49
K <sub>s</sub>	3	0".47
MS 1054-03		
J <sub>s</sub>	3.5	0".48
H	3	0".46
K <sub>s</sub>	3	0".53

NOTE. — Col. (1): Filters used. Col. (2) and Col. (3)  $\beta$  and FWHM values estimated by fitting a Moffat PSF to star profiles in the NIR images.

TABLE 2  
ANALYTICAL DESCRIPTIONS OF THE RESULTS OF  
OUR STRUCTURAL PARAMETER SIMULATIONS

$P_{re}$	$Q_{re}$	$P_n$	$Q_n$	$P_m$	$K_s$	$n_{input}$
1.01	1.00	1.01	0.95	0.01	20–21	<2.5
0.95	0.97	0.98	0.81	0.01	21–22	<2.5
0.84	0.87	0.89	0.65	0.03	22–23	<2.5
0.90	0.94	1.06	0.90	0.04	20–21	>2.5
0.60	0.76	1.03	0.68	0.12	21–22	>2.5
0.55	0.71	0.67	0.74	0.16	22–23	>2.5

NOTE. — Cols. (1)–(5): Values of the parameters used in the analytical fits to describe the difference between the input and the output  $r_e$  and  $n$  in our simulations. Col. (6)  $K_s$  band magnitude bin. Col. (7) Value of the input index  $n$ .

TABLE 3  
 PROPERTIES OF THE MS1054-03 SAMPLE GALAXIES

Galaxy	$K_{s,tot}$	$a_e$	$n$	$\epsilon$	$L_V(10^{10} h_{70}^{-2} L_{\odot})$	$M(10^{10} h_{70}^{-2} M_{\odot})$	$z$	Filter
1258	20.48	0.17	2.18	0.56	4.34	21.47	1.020	J <sub>s</sub>
355	21.76	0.76	1.02	0.48	1.37	2.93	1.020	J <sub>s</sub>
1638	22.64	0.17	3.06	0.48	0.54	1.56	1.040	J <sub>s</sub>
848	22.01	0.56	0.52	0.76	1.13	1.77	1.040	J <sub>s</sub>
1055	22.59	0.34	1.52	0.06	0.60	1.83	1.060	J <sub>s</sub>
1132	20.87	0.53	1.32	0.56	2.51	9.03	1.060	J <sub>s</sub>
1434	21.93	0.28	3.45	0.38	1.56	2.84	1.060	J <sub>s</sub>
1566	21.78	0.48	0.92	0.80	1.02	3.66	1.060	J <sub>s</sub>
1575	22.41	0.26	0.71	0.72	1.53	1.09	1.060	J <sub>s</sub>
1801	21.36	0.12	3.15	0.17	2.44	7.71	1.070	J <sub>s</sub>
830	22.29	0.31	1.05	0.52	1.51	1.23	1.073	J <sub>s</sub>
1401	20.41	0.40	1.51	0.36	8.68	4.52	1.075	J <sub>s</sub>
714	20.70	0.57	1.08	0.56	3.21	7.39	1.076	J <sub>s</sub>
1229	22.78	0.33	0.83	0.24	1.37	1.37	1.080	J <sub>s</sub>
1497	22.65	0.53	1.33	0.75	1.43	1.14	1.080	J <sub>s</sub>
178	22.25	0.41	0.99	0.73	2.10	1.21	1.080	J <sub>s</sub>
862	22.53	0.97	0.03	0.72	0.62	1.31	1.080	J <sub>s</sub>
617	20.68	1.12	2.40	0.54	4.43	19.59	1.100	J <sub>s</sub>
1216	21.29	0.12	3.96	0.50	2.70	15.27	1.120	J <sub>s</sub>
147	22.33	0.35	0.57	0.53	1.38	2.39	1.120	J <sub>s</sub>
150	22.55	0.20	1.00	0.48	1.54	2.55	1.120	J <sub>s</sub>
1768	21.28	0.54	1.31	0.56	2.50	7.41	1.120	J <sub>s</sub>
359	22.59	0.72	0.81	0.64	1.38	1.07	1.120	J <sub>s</sub>
100	21.13	0.15	3.54	0.51	3.09	15.69	1.140	J <sub>s</sub>
1172	22.50	0.14	4.04	0.36	0.91	6.68	1.140	J <sub>s</sub>
460	22.31	0.52	0.05	0.59	2.16	1.14	1.140	J <sub>s</sub>
527	21.02	0.46	5.31	0.28	3.36	16.33	1.140	J <sub>s</sub>
749	21.15	0.30	6.00	0.39	3.74	9.72	1.140	J <sub>s</sub>
1440	22.18	0.55	1.17	0.49	2.44	2.75	1.160	J <sub>s</sub>
1785	20.05	0.33	2.94	0.88	11.31	32.58	1.170	J <sub>s</sub>
494	21.87	0.20	6.24	0.38	2.44	3.15	1.175	J <sub>s</sub>
1273	22.15	0.14	3.35	0.26	2.12	1.82	1.180	J <sub>s</sub>
481	21.81	0.38	4.42	0.46	1.89	7.74	1.180	J <sub>s</sub>
1535	21.75	0.66	0.50	0.20	1.77	0.98	1.182	J <sub>s</sub>
508	21.49	1.10	0.46	0.87	1.61	5.76	1.189	J <sub>s</sub>
1301	21.91	0.15	2.88	0.26	1.83	30.94	1.200	J <sub>s</sub>
161	20.44	0.26	6.68	0.74	7.38	7.31	1.200	J <sub>s</sub>
1786	21.46	0.15	4.00	0.23	2.82	25.32	1.200	J <sub>s</sub>
1621	21.85	0.63	0.15	0.62	2.50	4.93	1.220	J <sub>s</sub>
306	20.90	0.77	3.29	0.23	6.66	5.47	1.220	J <sub>s</sub>
45	22.36	0.59	0.96	0.41	2.07	1.73	1.220	J <sub>s</sub>
614	20.75	0.37	1.78	0.37	5.26	11.28	1.220	J <sub>s</sub>
441	20.52	0.50	3.52	0.60	6.88	17.65	1.230	J <sub>s</sub>
1176	22.88	0.23	2.97	0.12	1.61	0.85	1.234	J <sub>s</sub>
743	22.48	0.13	4.45	0.41	1.11	5.88	1.240	J <sub>s</sub>
774	21.97	0.63	0.79	0.32	3.03	3.36	1.240	J <sub>s</sub>
1474	21.93	0.74	1.02	0.21	3.72	2.56	1.245	J <sub>s</sub>
1267	22.45	0.96	6.08	0.34	0.92	0.53	1.246	J <sub>s</sub>
1438	21.71	0.53	0.85	0.55	3.23	3.43	1.247	J <sub>s</sub>
1266	22.34	0.35	0.67	0.66	1.64	2.95	1.280	J <sub>s</sub>
1280	22.05	0.07	4.38	0.40	2.95	3.75	1.280	J <sub>s</sub>
737	21.09	0.59	1.54	0.69	6.09	9.31	1.280	J <sub>s</sub>
1226	22.87	0.41	0.70	0.67	1.64	0.79	1.295	J <sub>s</sub>
1256	20.50	0.46	1.55	0.14	10.30	22.85	1.300	J <sub>s</sub>
1637	21.77	1.01	0.96	0.85	1.89	3.52	1.300	J <sub>s</sub>
487	22.51	2.12	0.38	0.85	1.10	1.77	1.300	J <sub>s</sub>
54	21.78	0.65	0.94	0.61	3.60	3.94	1.300	J <sub>s</sub>
869	22.51	0.25	1.03	0.75	1.84	1.96	1.300	J <sub>s</sub>
971	22.98	0.20	1.16	0.91	0.93	1.52	1.300	J <sub>s</sub>
1071	21.52	0.18	4.30	0.51	3.50	16.62	1.320	J <sub>s</sub>
1456	21.58	0.13	6.00	0.54	5.36	2.77	1.320	J <sub>s</sub>
438	22.17	0.46	1.00	0.26	3.31	2.03	1.320	J <sub>s</sub>
67	21.06	0.55	3.35	0.23	7.06	6.20	1.326	J <sub>s</sub>
1120	22.68	0.67	0.38	0.47	2.09	1.02	1.340	J <sub>s</sub>
1218	22.21	1.10	0.10	0.81	3.17	2.54	1.340	J <sub>s</sub>
479	22.60	0.78	1.31	0.76	1.61	1.86	1.340	J <sub>s</sub>
732	22.61	0.55	0.96	0.27	1.94	1.12	1.360	J <sub>s</sub>
795	21.68	0.58	0.46	0.56	3.01	8.46	1.360	J <sub>s</sub>
845	21.79	0.53	0.56	0.13	4.46	2.88	1.360	J <sub>s</sub>
1719	20.79	0.40	2.10	0.21	7.73	18.70	1.400	J <sub>s</sub>
1763	22.17	0.27	1.89	0.36	2.90	4.03	1.400	J <sub>s</sub>
1781	21.21	0.18	4.00	0.20	4.95	28.18	1.400	J <sub>s</sub>
1249	22.53	1.05	0.02	0.75	2.71	2.26	1.420	J <sub>s</sub>
379	22.80	0.73	0.47	0.76	1.91	1.42	1.420	J <sub>s</sub>
552	22.32	0.60	0.66	0.74	2.48	3.09	1.420	J <sub>s</sub>
40	22.20	0.91	1.40	0.54	1.85	4.36	1.440	J <sub>s</sub>
1341	22.51	0.33	0.39	0.26	2.30	2.80	1.460	J <sub>s</sub>
1792	22.10	1.19	1.09	0.49	2.28	8.61	1.460	J <sub>s</sub>
259	22.93	0.31	0.78	0.42	1.96	1.17	1.460	J <sub>s</sub>
893	22.35	1.08	0.88	0.68	4.78	4.54	1.460	J <sub>s</sub>

TABLE 4  
 PROPERTIES OF THE HDF-S SAMPLE GALAXIES

Galaxy	$K_{s,tot}$	$a_e$	n	$\epsilon$	$L_V(10^{10} h_{70}^{-2} L_{\odot})$	$M(10^{10} h_{70}^{-2} M_{\odot})$	z	Filter
224	21.83	0.25	1.27	0.25	1.16	2.22	1.020	J <sub>s</sub>
753	22.90	0.23	1.02	0.26	0.84	0.60	1.020	J <sub>s</sub>
10008	22.33	0.15	2.13	0.36	0.66	2.16	1.040	J <sub>s</sub>
152	23.00	0.37	0.84	0.17	0.88	0.64	1.060	J <sub>s</sub>
241	21.72	0.74	1.19	0.56	1.51	3.20	1.060	J <sub>s</sub>
79	21.49	0.56	0.70	0.53	2.53	2.83	1.080	J <sub>s</sub>
18	21.20	0.31	1.12	0.36	2.24	6.71	1.100	J <sub>s</sub>
249	22.60	0.78	1.81	0.67	0.60	1.29	1.100	J <sub>s</sub>
565	20.75	0.48	0.87	0.28	4.72	5.98	1.114	J <sub>s</sub>
686	21.06	0.32	1.61	0.03	3.21	5.77	1.116	J <sub>s</sub>
493	20.97	0.36	4.57	0.55	3.29	4.14	1.120	J <sub>s</sub>
45	20.89	0.18	3.19	0.09	4.16	8.34	1.140	J <sub>s</sub>
206	22.71	0.37	0.48	0.37	1.37	0.68	1.152	J <sub>s</sub>
276	20.89	0.23	1.95	0.63	4.10	12.52	1.160	J <sub>s</sub>
644	22.67	0.22	0.85	0.18	0.83	4.58	1.160	J <sub>s</sub>
669	23.27	0.47	0.35	0.07	0.95	0.47	1.200	J <sub>s</sub>
404	22.75	0.49	0.55	0.27	1.33	1.22	1.220	J <sub>s</sub>
27	20.22	0.48	3.21	0.17	8.68	16.44	1.230	J <sub>s</sub>
251	22.79	0.67	0.61	0.76	1.11	1.45	1.240	J <sub>s</sub>
254	20.31	0.22	3.11	0.04	10.13	15.94	1.270	J <sub>s</sub>
101	22.23	0.37	2.16	0.63	2.48	2.94	1.280	J <sub>s</sub>
149	23.18	0.24	0.75	0.41	0.61	1.53	1.280	J <sub>s</sub>
470	20.39	0.49	0.84	0.14	8.03	12.52	1.284	J <sub>s</sub>
502	23.20	0.84	0.91	0.70	0.69	0.96	1.300	J <sub>s</sub>
771	22.86	0.25	0.46	0.33	0.92	1.41	1.300	J <sub>s</sub>
145	22.35	0.65	7.00	0.51	1.53	2.05	1.320	J <sub>s</sub>
395	22.65	0.25	0.56	0.15	1.84	1.75	1.320	J <sub>s</sub>
637	21.95	0.35	3.42	0.36	3.43	3.71	1.320	J <sub>s</sub>
199	21.68	0.27	2.90	0.25	2.64	12.80	1.340	J <sub>s</sub>
791	22.98	0.39	0.74	0.47	1.19	1.20	1.360	J <sub>s</sub>
437	23.16	0.68	1.05	0.71	1.19	1.19	1.380	J <sub>s</sub>
201	22.96	0.36	0.71	0.47	2.03	1.32	1.400	J <sub>s</sub>
408	23.09	0.16	1.68	0.59	1.54	1.15	1.400	J <sub>s</sub>
785	21.57	0.54	0.42	0.43	4.42	6.81	1.400	J <sub>s</sub>
751	23.13	0.19	0.97	0.14	1.41	1.65	1.420	J <sub>s</sub>
302	21.55	0.65	0.83	0.21	6.00	6.87	1.439	J <sub>s</sub>
10001	21.54	0.27	1.36	0.14	5.12	6.45	1.440	J <sub>s</sub>
61	23.03	0.78	3.42	0.45	1.20	1.39	1.440	J <sub>s</sub>
783	22.51	0.27	0.60	0.33	1.77	2.49	1.440	J <sub>s</sub>
781	22.73	0.77	1.10	0.66	2.21	1.53	1.480	J <sub>s</sub>
620	22.16	0.25	1.42	0.30	4.64	3.04	1.558	H
628	22.37	0.15	0.08	0.40	2.36	6.49	1.580	H
675	22.23	0.37	0.30	0.33	3.29	4.44	1.600	H
724	23.35	0.32	1.03	0.62	1.15	1.55	1.620	H
583	22.90	0.10	1.01	0.15	1.80	8.90	1.640	H
349	23.17	0.65	2.43	0.25	2.18	1.06	1.680	H
233	23.38	0.07	1.00	0.10	2.10	1.45	1.720	H
754	23.16	0.25	6.00	0.46	1.50	3.68	1.760	H
267	21.84	0.69	0.51	0.37	7.00	6.93	1.820	H
810	22.80	0.10	3.06	0.44	2.40	5.50	1.920	H
600	22.33	0.67	4.87	0.49	6.01	7.14	1.960	H
500	23.25	0.24	0.50	0.73	1.83	3.91	2.020	H
290	21.95	0.23	0.62	0.31	9.51	5.19	2.025	H
257	22.10	0.71	0.76	0.35	7.66	4.65	2.027	H
21	23.49	0.66	7.26	0.94	2.35	0.81	2.040	H
96	23.35	0.29	1.08	0.28	2.88	1.16	2.060	H
776	22.44	0.22	1.64	0.26	5.76	4.01	2.077	H
173	23.23	0.31	0.38	0.48	2.89	1.76	2.140	H
496	22.40	0.27	0.86	0.40	4.91	9.17	2.140	H
729	22.73	0.47	1.93	0.63	5.14	1.87	2.140	H
143	23.37	0.49	0.24	0.50	2.89	1.93	2.160	H
242	23.43	0.38	0.74	0.85	2.57	1.13	2.160	H
219	23.35	0.44	0.80	0.81	2.60	2.76	2.200	H
375	22.80	0.55	0.05	0.64	4.12	6.42	2.240	H
767	22.54	0.12	6.00	0.38	6.25	20.77	2.300	H
161	23.42	0.06	6.00	0.58	2.66	11.35	2.340	H
595	23.48	0.30	0.32	0.32	3.05	1.92	2.400	H
176	22.93	1.06	1.85	0.36	5.70	8.39	2.500	H
363	22.42	0.60	1.09	0.46	9.65	4.09	2.500	H
10006	23.32	0.10	4.90	0.18	4.97	2.88	2.652	K <sub>s</sub>
656	22.70	0.33	1.10	0.32	8.60	31.14	2.740	K <sub>s</sub>
452	22.84	0.44	0.36	0.55	8.45	6.25	2.760	K <sub>s</sub>
806	22.67	0.17	4.15	0.68	10.04	3.60	2.789	K <sub>s</sub>
807	22.70	0.28	0.87	0.30	9.93	3.80	2.790	K <sub>s</sub>
657	22.53	0.70	0.25	0.16	12.14	7.18	2.793	K <sub>s</sub>
294	23.34	0.45	0.36	0.35	5.74	3.99	2.820	K <sub>s</sub>
453	23.28	0.15	4.43	0.51	6.11	16.63	2.900	K <sub>s</sub>
494	23.00	0.72	1.78	0.47	9.14	4.67	3.000	K <sub>s</sub>
534	22.78	0.32	0.96	0.46	10.93	9.23	3.000	K <sub>s</sub>
487	22.88	0.35	0.52	0.52	6.82	6.82	3.040	K <sub>s</sub>

TABLE 5  
MEAN SIZE EVOLUTION VS REDSHIFT

$\langle z \rangle$	low-n	high-n
$L_V \gtrsim 3.4 \times 10^{10} h_{70}^{-2} L_{\odot}$		
0.1	1	1
0.3	$0.88 \pm 0.13$	$0.85 \pm 0.15$
0.5	$0.80 \pm 0.16$	$0.70 \pm 0.15$
0.65	$0.79 \pm 0.07$	$0.68 \pm 0.06$
0.9	$0.76 \pm 0.06$	$0.58 \pm 0.08$
1.2	$0.74 \pm 0.18$	$0.44 \pm 0.12$
1.7	$0.52 \pm 0.12$	$0.36 \pm 0.22$
2.5	$0.33 \pm 0.06$	$0.37 \pm 0.20$
$M_* \gtrsim 3 \times 10^{10} h_{70}^{-2} M_{\odot}$		
0.1	1	1
0.3	$0.88 \pm 0.14$	$0.92 \pm 0.11$
0.5	$0.84 \pm 0.09$	$0.76 \pm 0.08$
0.65	$0.90 \pm 0.05$	$0.86 \pm 0.06$
0.9	$0.90 \pm 0.07$	$0.84 \pm 0.10$
1.2	$0.81 \pm 0.13$	$0.65 \pm 0.18$
1.7	$0.67 \pm 0.16$	$0.69 \pm 0.32$
2.5	$0.54 \pm 0.10$	$0.71 \pm 0.50$

NOTE. — Col. (1): Mean redshift of the bin  
Col. (2) and Col. (3)  $r_e(z)/r_e(0.1)$  and the  $2\sigma$   
uncertainty on the mean values estimated from  
the  $\log(r_{e,c}/r_{e,SDSS})$  distribution.



TABLE 6  
ANALYTICAL FITS TO THE SIZE EVOLUTION

Fit	$\alpha$	$\tilde{\chi}^2$
$L_V \gtrsim 3.4 \times 10^{10} h_{70}^{-2} L_{\odot}$ (low-n)		
$(1+z)^{\alpha}$	$-0.84 \pm 0.05$	2.29
$H^{\alpha}(z)$	$-0.83 \pm 0.05$	0.71
$L_V \gtrsim 3.4 \times 10^{10} h_{70}^{-2} L_{\odot}$ (high-n)		
$(1+z)^{\alpha}$	$-1.01 \pm 0.08$	0.25
$H^{\alpha}(z)$	$-1.13 \pm 0.09$	0.68
$M_{\star} \gtrsim 3 \times 10^{10} h_{70}^{-2} M_{\odot}$ (low-n)		
$(1+z)^{\alpha}$	$-0.40 \pm 0.06$	0.89
$H^{\alpha}(z)$	$-0.43 \pm 0.07$	0.50
$M_{\star} \gtrsim 3 \times 10^{10} h_{70}^{-2} M_{\odot}$ (high-n)		
$(1+z)^{\alpha}$	$-0.45 \pm 0.10$	0.59
$H^{\alpha}(z)$	$-0.54 \pm 0.12$	0.73

NOTE. — Col. (1): Analytical expression used to fit the data Col. (2) Value of the parameter measured including  $1\sigma$  error bar and Col. (3) Reduced  $\tilde{\chi}^2$  value of the fit.

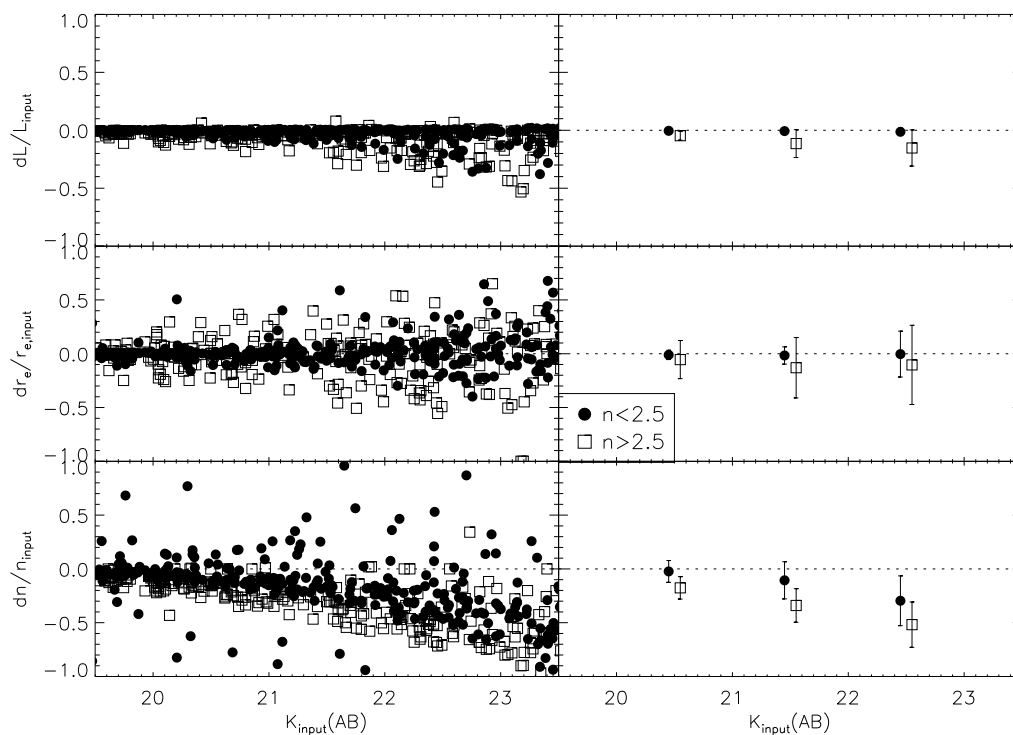


FIG. 1.— The relative error derived from the difference between the input and recovered structural parameters  $((\text{output}-\text{input})/\text{input})$  according to our simulations for the FIRES MS1054 field. Solid symbols are used to indicate less concentrated objects ( $n_{input} < 2.5$ ) whereas open symbols imply highly concentrated objects ( $n_{input} > 2.5$ ). The right column of plots shows the mean systematic difference and  $1\sigma$  error bars.

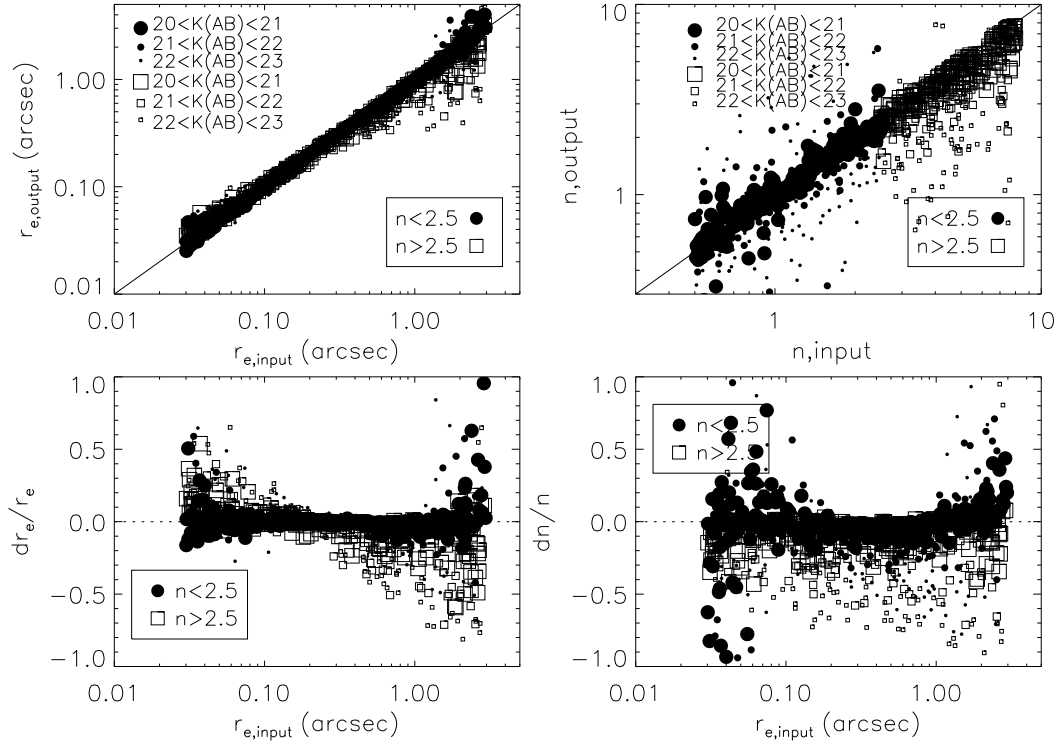


FIG. 2.— Galaxy size-measurement bias: The figure shows a comparison between input and recovered structural parameter values in our simulations for the FIRES observations of the MS1054 field. *Top Left:* The relation between measured and the input intrinsic half-light radius (before seeing convolution). *Top Right:* The relation between measured and input seeing deconvolved Sérsic index  $n$ . *Bottom Left:* The relative error between the input and the measured seeing deconvolved effective radius ( $dr_e/r_e = (r_{e,output} - r_{e,input})/r_{e,input}$ ) versus the input effective radius. *Bottom Right:* The relative error between the input and the measured seeing deconvolved Sérsic index  $n$  ( $dn/n = (n_{,output} - n_{,input})/n_{,input}$ ) versus the input effective radius. Solid symbols are used to indicate less concentrated objects ( $n_{input} < 2.5$ ) whereas open symbols imply highly concentrated objects ( $n_{input} > 2.5$ ).

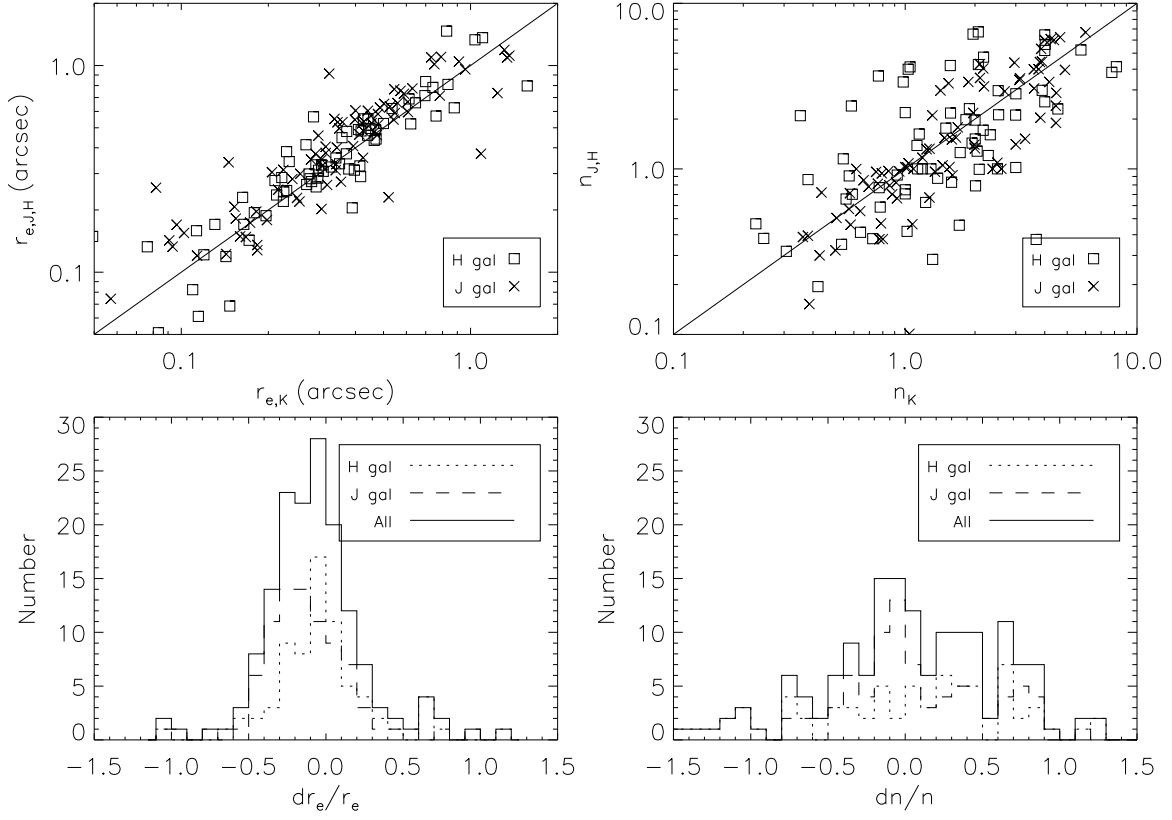


FIG. 3.— *Upper panels:* Comparison between the profile shapes and size estimates using the FIRES  $J_s$  or H filters versus the  $K_s$  band for all the galaxies in the MS1054 field with  $1 < z < 2.6$ . To match the rest-frame optical V-band, galaxies with  $1 < z < 1.5$  were observed in the  $J_s$ -band, and galaxies with  $1.5 < z < 2.6$  were observed in the H-band. *Lower panels:* The relative difference between the size and the shape parameter measured in the different filters:  $dr_e/r_e = 2 \times (r_{e,K} - r_{e,J,H}) / (r_{e,K} + r_{e,J,H})$  and  $dn/n = 2 \times (n_K - n_{J,H}) / (n_K + n_{J,H})$ . The standard deviation for the sizes is  $\sim 24\%$  and for the shapes  $\sim 60\%$ .

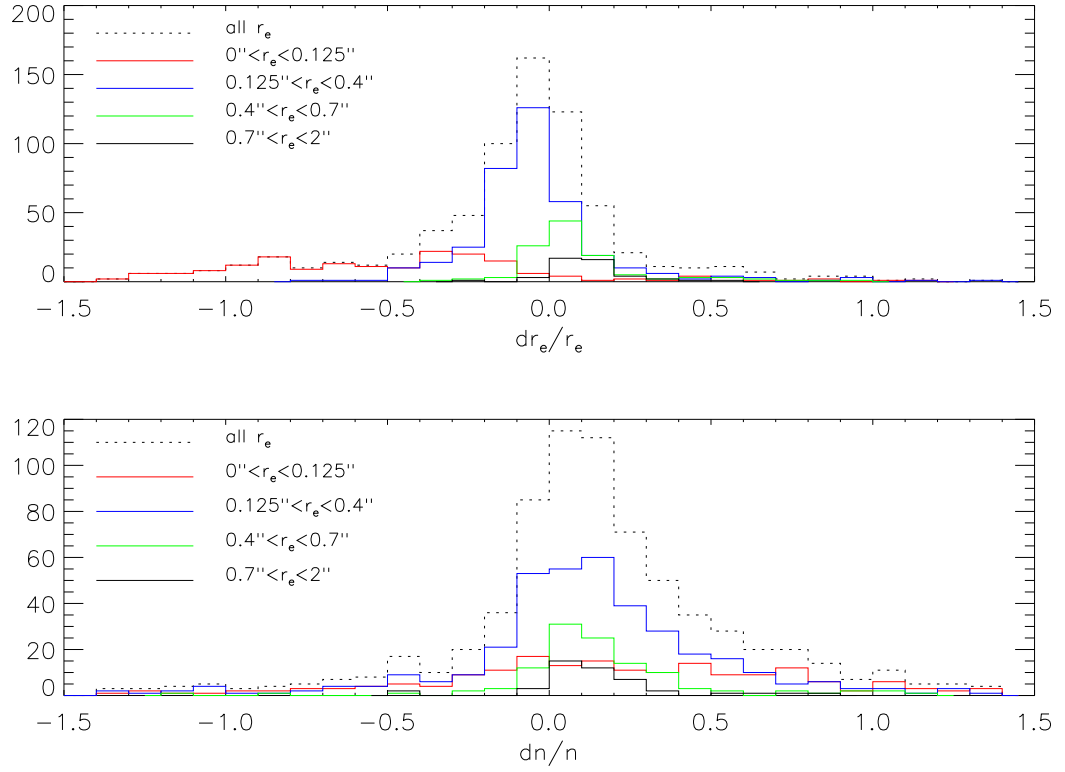


FIG. 4.— Reliability of the structural parameter estimation using different PSFs. *Top Panel.* The relative difference between the circularised sizes estimated in the  $K_s$  using a PSF with a FWHM equal to the median value of the different PSFs (PSF1) and the size measured using a PSF with a FWHM  $2\sigma$  times larger than the median (PSF2).  $dr_e/r_e = 2 \times (r_{e,PSF2} - r_{e,PSF1}) / (r_{e,PSF2} + r_{e,PSF1})$ . *Bottom Panel.* Same than in the top panel for the Sérsic index  $n$ :  $dn/n = 2 \times (n_{PSF2} - n_{PSF1}) / (n_{PSF2} + n_{PSF1})$ .

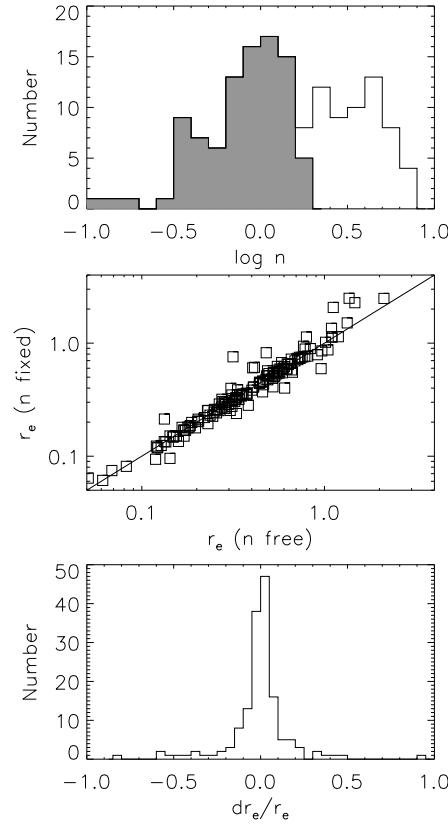


FIG. 5.— *Top Panel.* The grey histogram shows the Sérsic index distribution (when leaving this parameter free in the fitting process) for the subset of galaxies which are better fit with a fixed Sérsic parameter to  $n=1$  whereas the open histogram shows the shape distribution for the galaxies well fitted with  $n=4$ . *Center Panel.* The comparison between the size estimated using  $n$  free versus the size estimated using  $n$  fixed to 1 or 4. *Bottom Panel.* The relative difference between the size estimated using  $n$  fixed or free:  $dr_e/r_e = 2 \times (r_{e,n \text{ free}} - r_{e,n \text{ fixed}}) / (r_{e,n \text{ free}} + r_{e,n \text{ fixed}})$ . The scatter between both sizes estimates is  $\sim 7\%$  ( $1\sigma$ ). The structural parameters are estimated using the filters which match the V-band restframe at every  $z$ .

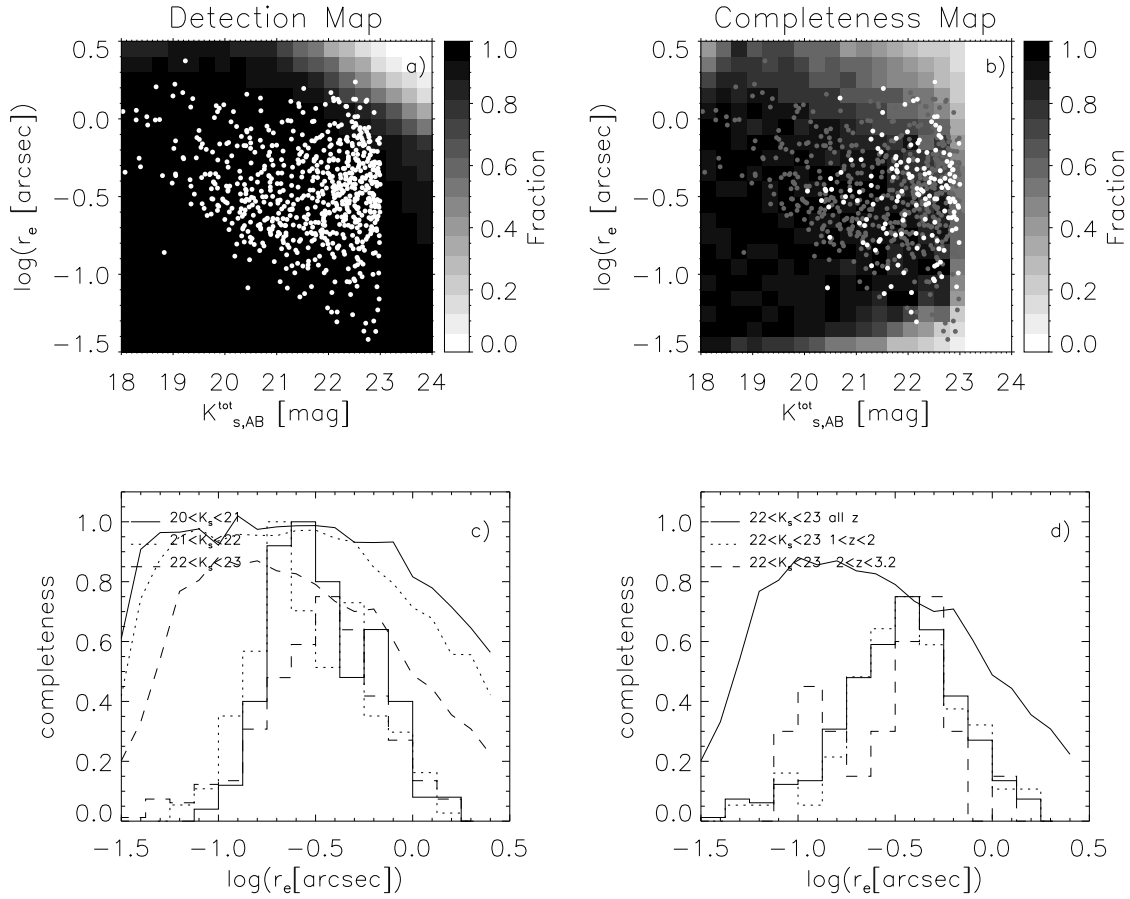


FIG. 6.— *a*) Detection map for simulated sources with exponential profiles placed at random in our  $K_s$  band image of the MS1054 field. The grey-scale map reflects the ratio between input and recovered objects per input magnitude and  $\log(r_e)$  bin. Overplotted on the map is the distribution of the full sample of  $K_s$  band selected objects in the MS1054 field. *b*) Completeness map for simulated sources with exponential profiles placed at random in our  $K_s$  band image of the MS1054 field. The grey-scale map reflects the ratio between the number of output galaxies with recovered magnitude and size at a given magnitude and  $\log(r_e)$  bin and the number of input galaxies with input magnitude and size in that bin. Overplotted on the map is the distribution of the full sample of  $K_s$  band selected objects in the MS1054 field with those explored in this paper ( $1 < z < 3.2$ ) highlighted. *c*) The completeness for three different magnitude intervals:  $20 < K_s < 21$ ,  $21 < K_s < 22$  and  $22 < K_s < 23$  as a function of the size (smooth curves). Overplotted are the size distributions (arbitrarily normalized to have a value at the peaks equal to the completeness value provided by the completeness curve at that  $r_e$ ) of real galaxies in the same intervals (histograms). *d*) The completeness for our faintest magnitude interval  $22 < K_s < 23$  as a function of the size (smooth curve). Overplotted are the apparent size distributions (arbitrarily normalized to have a value of 0.75 in the peak) of real galaxies in the same interval (histograms) for: all the galaxies, galaxies with  $1 < z < 2$  and galaxies with  $2 < z < 3.2$ . The apparent size distribution of the galaxies in this magnitude interval is independent of redshift. The observed size distribution decline more rapidly to larger sizes than the completeness limit. This indicates that our sample is not significantly affected by incompleteness of the largest galaxies at a given magnitude.

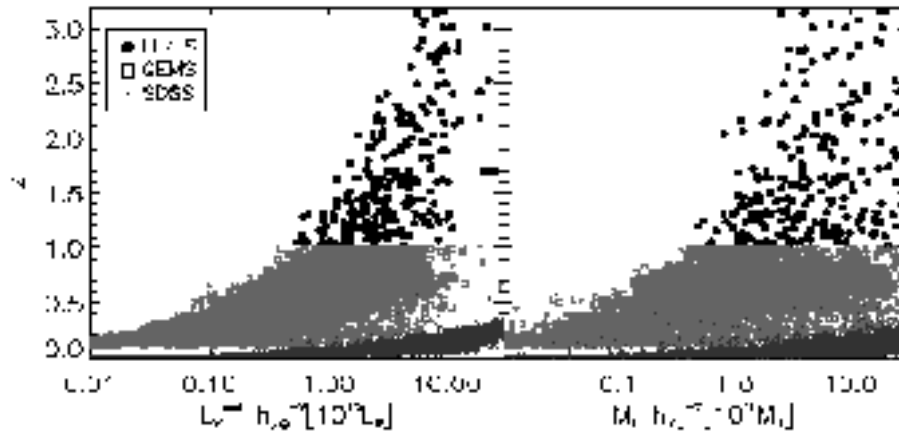


FIG. 7.— The  $L_V$ - $z$  and  $M_*$ - $z$  diagrams for the combined data set used in the present analysis. Solid points correspond to the FIRES galaxies in the HDF-S and the MS1054 fields, open squares are GEMS galaxies (McIntosh et al. 2005; Barden et al. 2005) and dots are the SDSS galaxies (Shen et al. 2003). Only the most luminous and the most massive objects can be homogeneously explored along the full redshift range. Since the mean redshift is our highest redshift bin is  $\sim 2.5$ , only galaxies with  $L_V \gtrsim 3.4 \times 10^{10} h_{70}^{-2} L_{\odot}$  can be studied as a homogeneous sample. Objects with the lowest mass-to-light ratios can be homogeneously explored if their masses are  $M_* \gtrsim 3 \times 10^{10} h_{70}^{-2} M_{\odot}$ . We are complete to objects of every stellar mass-to-light ratio if  $M_* \gtrsim 6.6 \times 10^{10} h_{70}^{-2} M_{\odot}$  (see text for details).



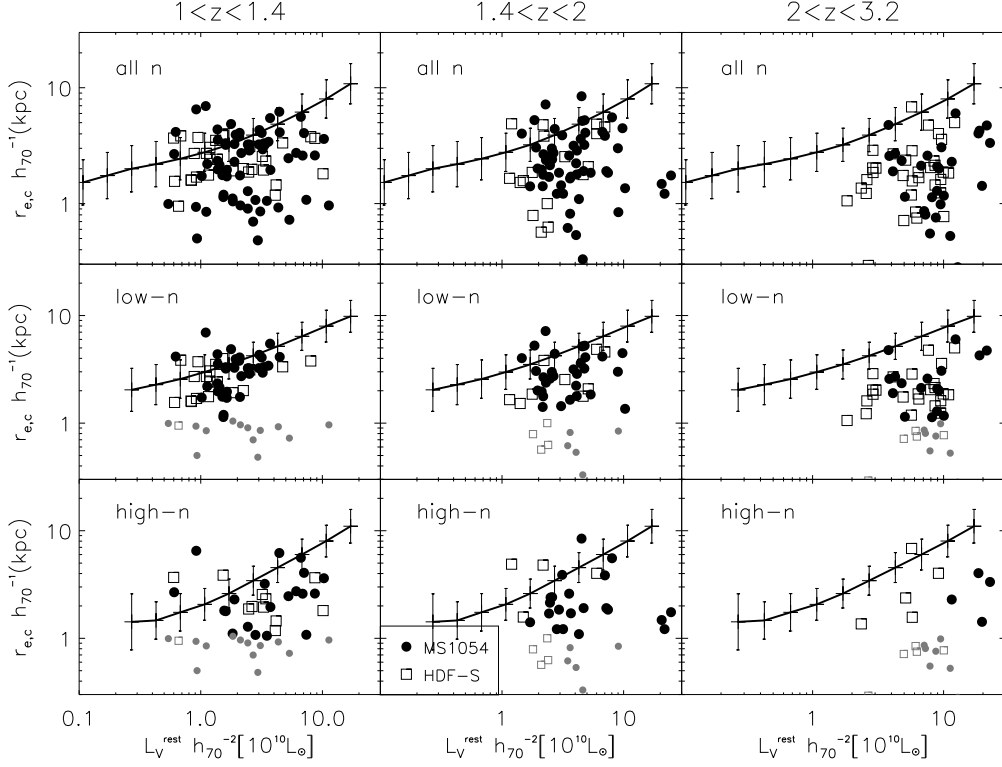


FIG. 8.— Distribution of the rest-frame optical sizes vs. the rest-frame V-band luminosities for all galaxies from FIRES. Galaxies from the HDF-S field (Labbé et al. 2003) are shown by open squares and galaxies from the MS1054 field (Förster Schreiber et al. 2005) by filled circles. The different rows show the galaxies separated according to their Sérsic index concentration parameter. For objects with  $r_e < 0.''125$  the estimation of the Sérsic index  $n$  is uncertain. For that reason, these objects are plotted simultaneously in the low and high- $n$  rows using lighted symbols. Overplotted on the observed distribution of points are the mean and dispersion of the distribution of the Sérsic half-light radius of the SDSS galaxies (in the “V-band”) as a function of the V-band luminosity. The second and third row show the SDSS distributions separating into late and early type respectively. For clarity individual error bars for the FIRES data are not shown; the mean size relative error is 25%.

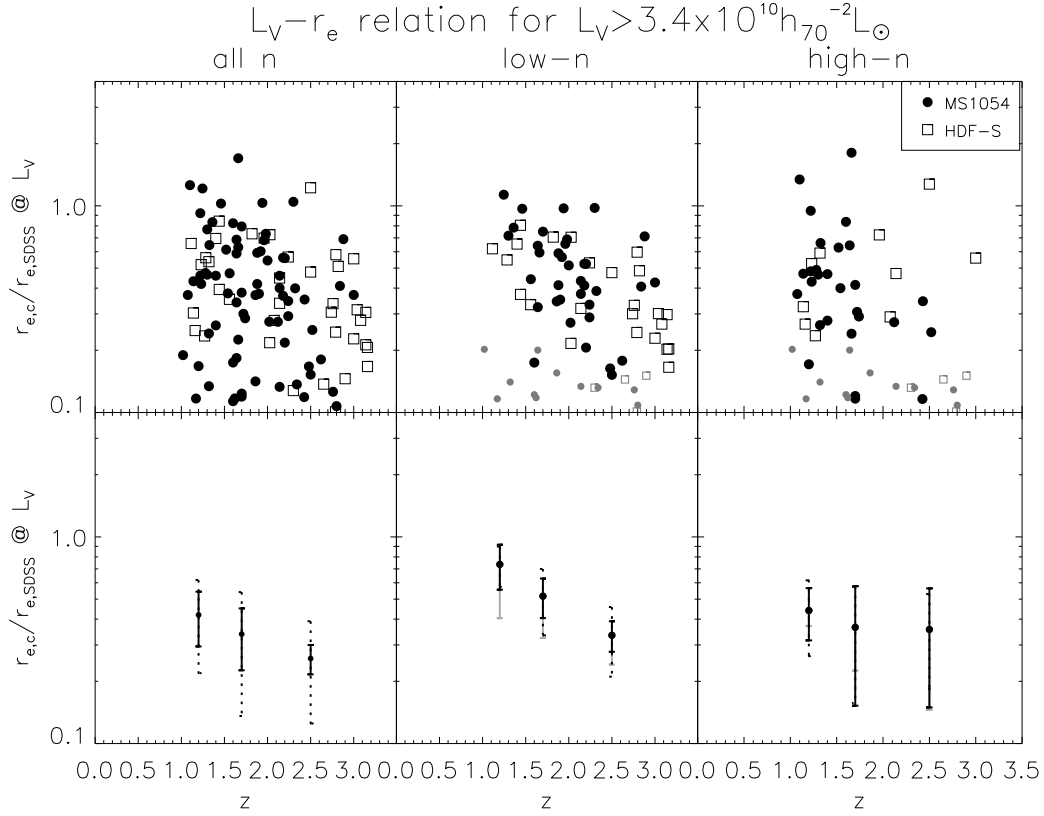


FIG. 9.— Redshift evolution of the size–luminosity relation for FIRES galaxies: the figure shows the ratio between the observed size (at a given luminosity) and the mean size of equally luminous present–day galaxies from the local SDSS sample as a function of  $z$ . For objects with  $r_e < 0.''125$  the estimation of the Sérsic index  $n$  is uncertain. For that reason, these objects are plotted simultaneously in the low and high- $n$  rows using lighted symbols. The upper panels show the individual objects whereas the lower panels show the dispersion (dotted error bars) and the uncertainty ( $2\sigma$ ) in the mean determination (solid error bars) estimated from the  $\log(r_{e,c}/r_{e,SDSS})$  distribution. Grey error bars show how the contribution of the small galaxies could affect the estimation of the mean. The figure shows that galaxies of a given luminosity were physically smaller at early epochs (or higher redshift). Alternatively, the plot shows that galaxies of a given size were more luminous at higher  $z$ .

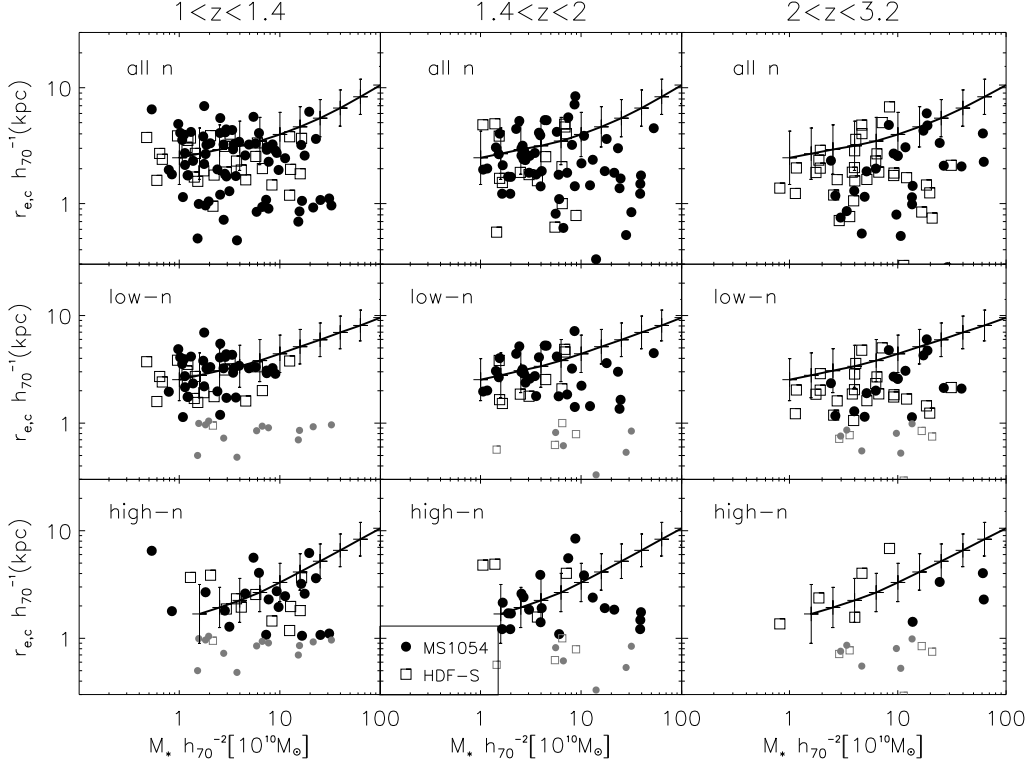


FIG. 10.— Distribution of rest-frame optical sizes vs. the stellar masses for FIRES galaxies. Analogously to Fig. 8 galaxies from the HDF-S field are shown by open squares and galaxies from the MS1054 field by filled circles. The different rows show the galaxies separated according to their Sérsic index shape parameter. For objects with  $r_e < 0.''125$  the estimation of the Sérsic index  $n$  is uncertain. For that reason, these objects are plotted simultaneously in the low and high- $n$  rows using lighted symbols. Overplotted on the observed distribution of points are the mean and dispersion of the distribution of the Sérsic half-light radius of the SDSS galaxies as a function of the stellar mass. The second and third row show the SDSS distributions separated into late and early type respectively. For clarity, individual error bars are not shown. The mean size relative error is 25%.

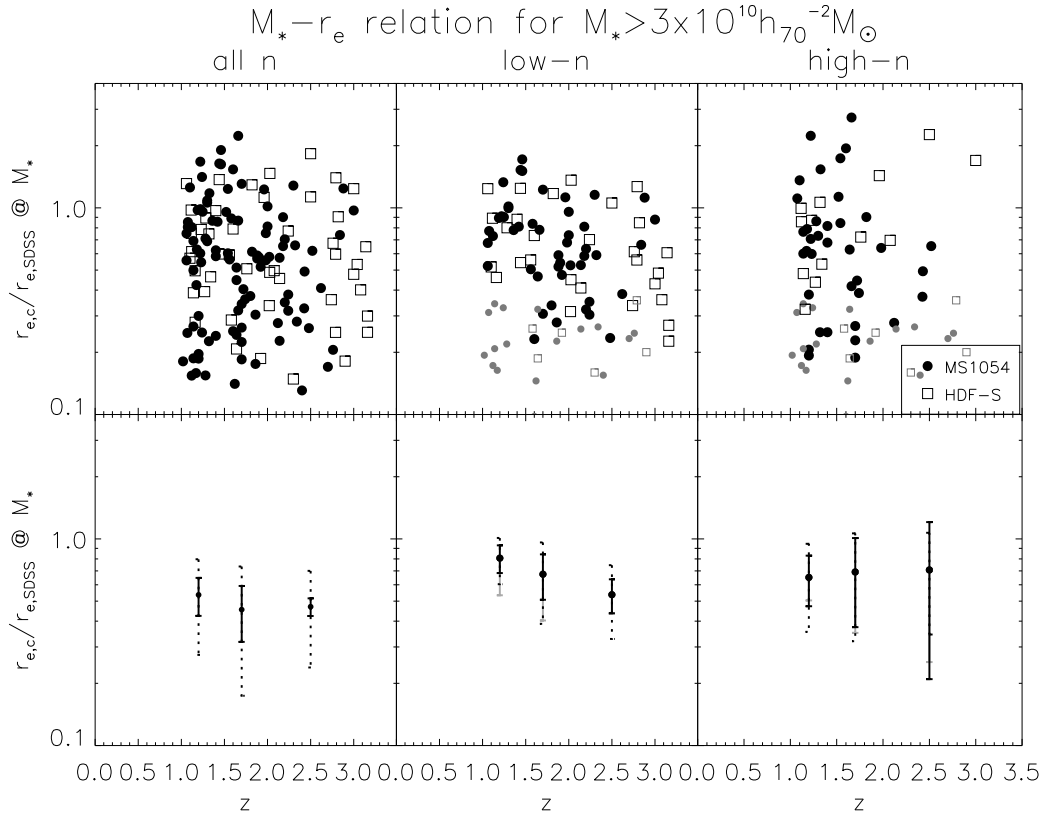


FIG. 11.— The ratio between observed size of FIRES galaxies and the size (at a given stellar mass) expected from the local SDSS sample shown as a function of  $z$ . The upper panels show the individual objects whereas the lower panels show the dispersion (dotted error bars) and the uncertainty ( $2\sigma$ ) at the mean determination (solid error bars) estimated from the  $\log(r_{e,c}/r_{e,SDSS})$  distribution. Grey error bars show how the contribution of the small galaxies could affect the estimation of the mean. The size at a given mass evolves moderately with  $z$ .

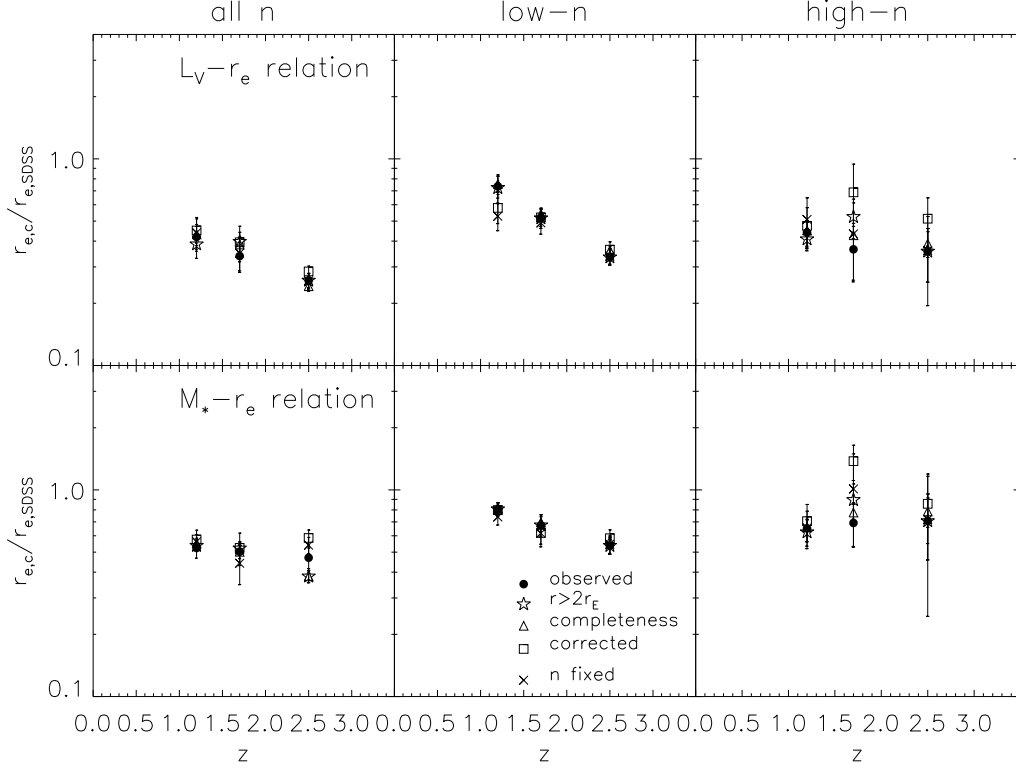


FIG. 12.— Comparison between five different estimates of the mean luminosity– and stellar mass–size distributions: the direct estimates (solid points), the estimates omitting the galaxies inside two Einstein radii ( $r_E \sim 15''$ ; Hoekstra et al. 2000) of the MS1054 cluster (open stars), the estimation weighting every galaxy according to the completeness map (open triangles), the estimation using the corrections suggested from our simulations (open squares) and the estimation using fits where the Sérsic index  $n$  is fixed to 1 or 4 (crosses). The error bars show the  $1\sigma$  uncertainty in estimating the mean of the distributions. All the points are in agreement within  $\sim 1\sigma$ . For clarity, bars showing the intrinsic dispersion of the relations are not included.

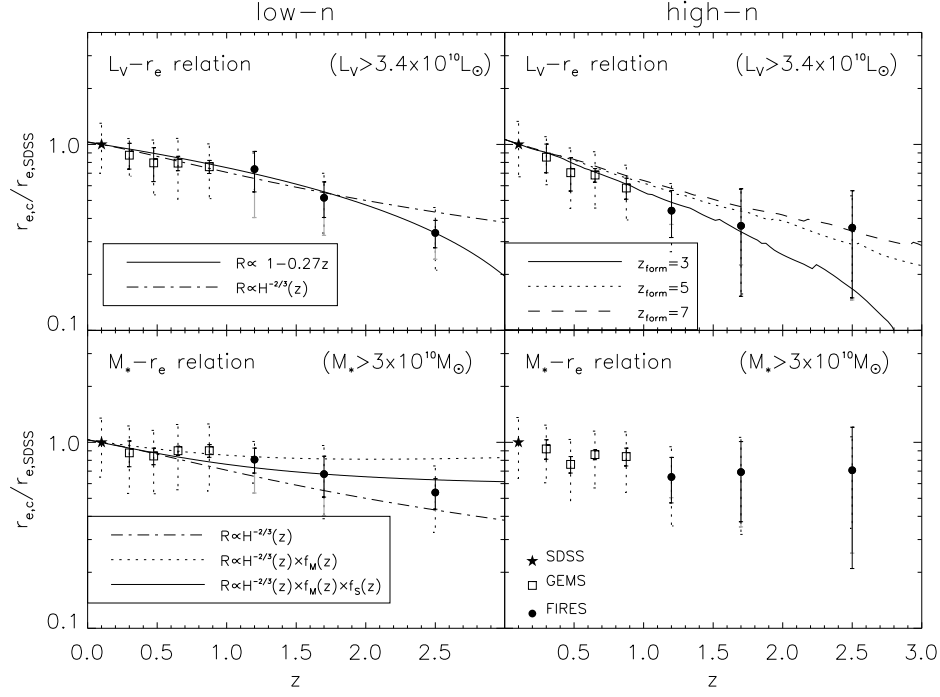


FIG. 13.— Redshift evolution of the ratio between the observed size and the present–day mean size at a given luminosity (upper panels), and the analogous ratio at a given mass (lower panels). The present–day values are derived from the SDSS sample (Shen et al. 2003). The comparison is restricted to the luminous ( $L_V \gtrsim 3.4 \times 10^{10} h_{70}^{-2} L_\odot$ ) and to massive ( $M_* \gtrsim 3 \times 10^{10} h_{70}^{-2} M_\odot$ ) galaxies. Open squares correspond to the GEMS sample (McIntosh et al. 2005; Barden et al. 2005) for galaxies with  $z < 1$  and solid points indicate the results from FIRES. The star indicates our local reference values from SDSS (mean  $z \sim 0.1$ ). We present the dispersion (dashed error bars) and the uncertainty ( $2\sigma$ ) at the mean determination (solid error bars) estimated from the  $\log(r_{e,c}/r_{e,SDSS})$  distribution. Grey error bars show how the contribution of the small galaxies could affect the estimation of the mean. *Left column*: The dashed lines illustrate the expected evolution (Mo et al. 1998) at a fixed halo mass  $R \propto H^{-2/3}(z)$  normalized to be 1 at  $z=0.1$ . The predicted size evolution at a given luminosity for Milky Way type objects (from the Bouwens & Silk 2002 infall model) is indicated with a solid line in the upper left panel. In the lower left panel we show (dotted line) the Mo et al. (1998) size evolution at a given halo mass corrected by the evolution of the stellar to halo mass  $f_M(z) = (M_{halo}/M_*)^{1/3}(z)$ . The solid line accounts for the transformation of the gas settled in the disk into stars by multiplying the above correction for an extra factor  $f_S(z) = R_*/R_{disk}(z)$ . *Right column*. The different lines illustrate the expected size evolution if the local luminosity–size relation for early–type galaxies is evolved in luminosity as expected for single–age stellar population models with different formation redshift (computed assuming a Salpeter 1955 IMF using the PEGASE (Fioc & Rocca–Volmerange 1997) code).

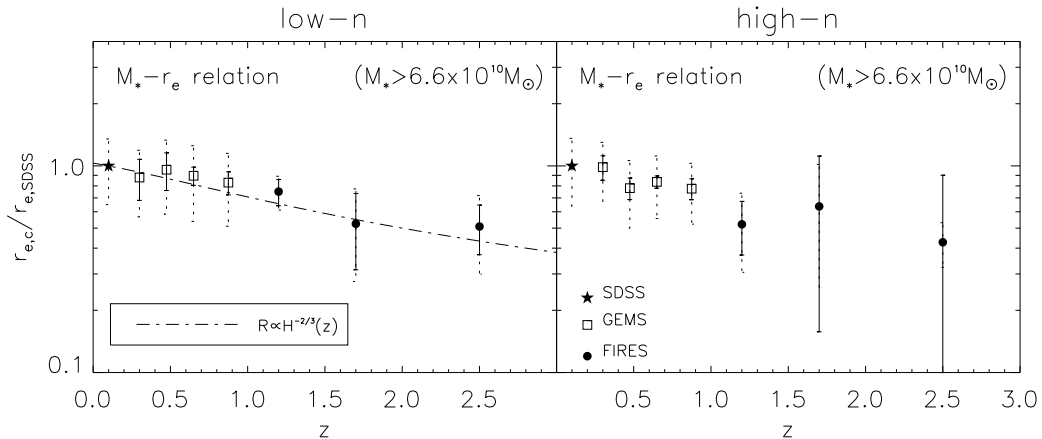


FIG. 14.— The ratio between observed size and expected size and at a given mass from the local SDSS sample (Shen et al. 2003) as a function of  $z$  for galaxies more massive than our completeness mass limit ( $M_* \gtrsim 6.6 \times 10^{10} h_{70}^{-2} M_\odot$ ). The meaning of the symbols is the same than in Fig. 13.